

# Investigation of the Two-Dimensional Harmonically Confined Bose Gas

Russell Bisset

October 5, 2007

A dissertation submitted in partial fulfilment for the degree of  
Bachelor of Science with Honours in Physics  
University of Otago, New Zealand

## **Abstract**

We begin by the introduction of 2D systems and their properties in the general sense. Focus then turns to the interacting trapped 2D regime in the context of the ultra-cold Bose gas. Details for the ideal cases and interacting homogenous case are investigated, and these results are discussed in terms of their possible implications to the interacting trapped system. We pose the question of the behaviour of the BKT transition.

We outline the motivation and numerical implementation of classical field simulations, followed by a discussion of the classical field energy cutoff.

We present numerical results that show how the properties of macroscopic parameters vary across the BKT transition, these parameters are momentum bimodality, vortex distribution and peak position density.

## **Acknowledgements**

Many thanks go to my supervisor Dr Blair Blakie, who is exceptional at explaining difficult concepts and has taught me so much.

Also, thanks to those who live in room 509 for the awesome year.

# Contents

<b>1</b>	<b>Introduction</b>	<b>4</b>
1.1	Overview of Ultra-Cold Bose Gases . . . . .	4
1.2	Phase Transitions in Two-Dimensional Systems . . . . .	5
1.3	Two-Dimensional Experimental Setups and Results . . . . .	7
1.4	Research Focus . . . . .	8
1.5	Chapter Overview . . . . .	9
<b>2</b>	<b>Phases of Two-Dimensional Bose Gases</b>	<b>10</b>
2.1	Ideal Gas Theory . . . . .	10
2.1.1	Ideal Homogeneous Case . . . . .	11
2.1.2	Ideal Harmonically Confined Case . . . . .	12
2.1.3	Critical Density for Ideal Gas BEC . . . . .	14
2.2	Berezinskii-Kosterlitz-Thouless Phase Transition . . . . .	16
2.2.1	Interacting 2D Trapped Regime . . . . .	16
2.2.2	Interacting 2D Homogeneous Regime . . . . .	16
2.2.3	Quasi-Condensate . . . . .	18
<b>3</b>	<b>Classical Field Simulations</b>	<b>19</b>
3.1	Energy Modes and Phase Transitions . . . . .	19
3.2	Motivation . . . . .	19
3.3	Classical Region Formalism . . . . .	20
3.4	Numerical Implementation . . . . .	22
3.4.1	Classical Region . . . . .	22
3.4.2	Incoherent Region . . . . .	23
3.5	Simulation Procedure . . . . .	24
3.5.1	Macroscopic Parameters . . . . .	24
3.5.2	Procedure . . . . .	24
3.5.3	Cutoff Energy . . . . .	25
3.5.4	Simulation Modes . . . . .	25
3.6	CFS Summary . . . . .	27

<b>4</b>	<b>Phase Results</b>	<b>28</b>
4.1	Results for Experimental Trap Parameters . . . . .	28
4.2	Characterisation of BKT Transition . . . . .	30
4.2.1	Parameters . . . . .	30
4.2.2	Bimodality in Momentum Distribution . . . . .	31
4.2.3	Peak Density in Position Space . . . . .	33
4.2.4	Condensation Fraction versus Temperature . . . . .	34
4.2.5	Phase Diagrams . . . . .	39
4.2.6	Vortices in Position Space . . . . .	39
4.3	Vortex Pair Dynamics in BKT Regime . . . . .	42
<b>5</b>	<b>Conclusions</b>	<b>46</b>
<b>6</b>	<b>Appendix</b>	<b>47</b>
6.1	Cutoff Predictions . . . . .	47
6.2	Cutoff Dependence . . . . .	48

# Chapter 1

## Introduction

### 1.1 Overview of Ultra-Cold Bose Gases

A Bose gas is a quantum mechanical system comprised of unbound bosons. For any system of finite extension, allowable energy states are discrete. Further, each state must contain an integer number of bosons, and the average occupation is given by the Bose-Einstein distribution 3.20. The ultra-cold regime is defined to be temperatures for which the mean occupation of single states becomes of order unity and quantum statistical mechanics becomes important.

The energy spectrum is of fundamental importance to behaviour of ultra-cold Bose gases. Hence, the confining potential is of extreme importance. This can be seen rather dramatically by considering the anisotropic three-dimensional (3D) harmonic potential. Let the confinement in one direction (tight) be much greater than that for the other two (loose). Set the temperature, such that the thermal energy is greater than the energy spacing of the loose directions but much smaller than that of the tight. In this regime, the excited states of the tight direction are “*frozen out*”, meaning their occupation is negligible. This regime is called a two-dimensional (2D) gas. The reduction of dimensionality has a profound effect on macroscopic behaviour. One-dimensional gases can also be obtained, but these are not considered here.

## 1.2 Phase Transitions in Two-Dimensional Systems

The phases of 3D systems are relatively well defined and insight to behaviour can be gained by simple arguments. At zero temperature, all system components are in the ground state. Hence there is complete “*off diagonal long range order*” ODLRO, indicating that two well-separated points in the system exhibit coherence, similar to the properties of a laser. With rising temperature, the ground state occupation falls rapidly until a critical temperature  $T_c$  is reached. This fundamental change that occurs at the phase transition is that for  $T < T_c$  the system has long range order. This order, which is a manifestation of the sudden increase in ground state occupation as temperature drops below  $T_c$ , is known as Bose-Einstein condensation and these ground state particles are collectively known as the Bose-Einstein condensate (BEC). For the thermal phase, above  $T_c$ , coherence between any two points decreases exponentially as a function of separation. We note that Bose-Einstein condensation is a second order phase transition.

The situation is much more complicated in 2D. First, consider the ideal homogenous system where the potential is constant everywhere. Unlike the usual 3D case, the density of states is such that the thermal cloud cannot be saturated for any finite number of atoms, thus BEC does not occur, except at  $T = 0$ . The addition of an externally applied harmonic potential to 2D systems, significantly modifies the density of states  $g(\epsilon)$ , so that BEC is now possible at some finite  $T_c$ .

Returning to the homogenous system we now consider interactions. In 1973 a new kind of *quasi-order* was described by Kosterlitz et al[11], for 2D interacting systems. Their name for this was *topological order*, due to the absence of long-range order but the presence of local coherence. More precisely, the coherence decreases algebraically with distance. Above a critical temperature  $T_{BKT}$ , the topological order is thought to diminish rapidly. This is known as the Kosterlitz Thouless phase transition for 2D. The microscopic mechanism proposed for this order is based on the pairing of vortices of opposite circulations. Isolated vortices create a large phase disturbance and are energetically costly. Vortex pairs reduce the phase disturbance by means of partial cancelation. This effect is particularly significant at large distances, analogous in this respect to an electric dipole. The breaking of vortex pairs at higher temperature is predicted to occur rapidly, the resulting *free* vortices are responsible for the swift destruction of topological order at  $T_{BKT}$ . From here on, topological order will be referred to as the Berezinskii-Kosterlitz-Thouless (BKT) phase, in recognition to those who developed this theory.

Finally, consider 2D systems that are both harmonically trapped and include interactions. This case is complicated, with macroscopic behaviour and microscopic mechanisms being poorly understood. There has been much speculation and one prominent idea proposes that BEC exists below  $T_c$ , while BKT occurs between  $T_c$  and  $T_{BKT}$  followed by a thermal phase above  $T_{BKT}$ . However, this is likely to be a simplification of the actual behaviour and  $T_c$  maybe a crossover temperature rather than a real phase transition. Additionally as the trap is relaxed and the system approaches the thermodynamic limit  $N \rightarrow \infty$  ( $N\omega^2 = \text{constant}$ ), then  $T_c \rightarrow 0$ , while  $T_{BKT}$  remains finite. These ideas are summarised by figure 1.1, the predictions for this phase diagram are based on free energy arguments from Hutchinson and coworkers[18]. Extensive work has been done on the coherence and properties of the BEC phase [9]. In the past 3 years 2D trapped gases have been experimentally realised and three important papers have been published by the ENS (Paris) group[10, 17, 12]. A debate is emerging, as how to interpret the results and reliable simulations have yet to be carried out to understand their results.

### Phase diagram of 2D trapped Bose gas

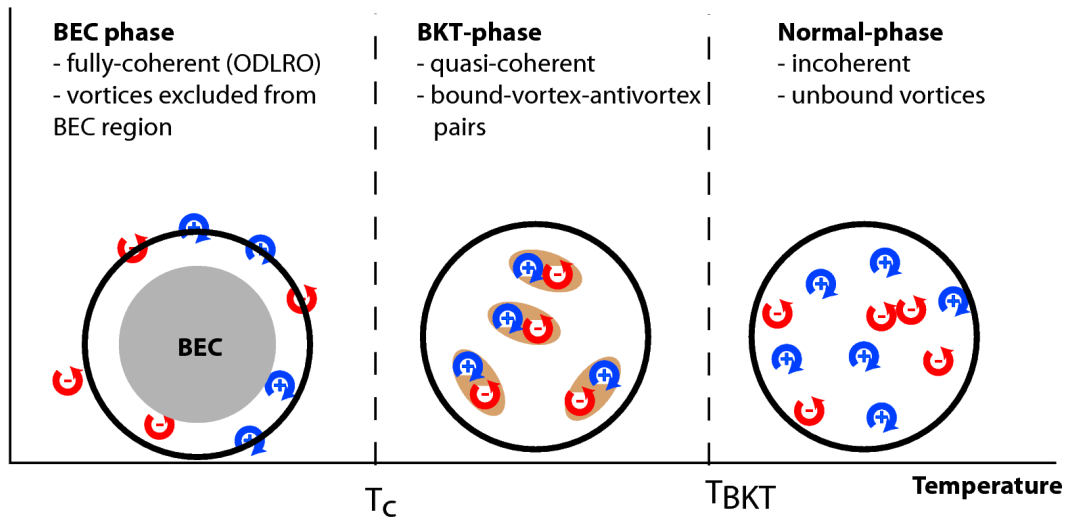


Figure 1.1: (Figure taken from Ref. [18]).

### 1.3 Two-Dimensional Experimental Setups and Results

We now briefly review the experiments in the 2D regime [10, 17, 12]. These experiments begin with a condensate of  $^{87}\text{Rb}$  atoms magnetically trapped in a cylindrically symmetric trap. The condensate is produced by radio-frequency (rf) evaporation and contains of order  $4 \times 10^5$  bosons. A one-dimensional (1D) optical lattice is applied in the vertical direction (figure 1.2), which divides the 3D cloud. This periodic potential compresses the individual regions, resulting in 2D systems as defined in §1.1.

The number of atoms contained within these *stacked* 2D systems can be reduced by rf induced evaporation. An additional magnetic field creates a gradient potential along the vertical direction. This has the effect of splitting the resonant frequencies, such that rf evaporation can selective address individual systems. Some experiments require only one 2D system, for example when looking at the momentum distribution. While *stacked* systems are used with each other to interfere several to study phase defects and coherence in 2D systems.

There have been three seminal experimental results which are relevant to

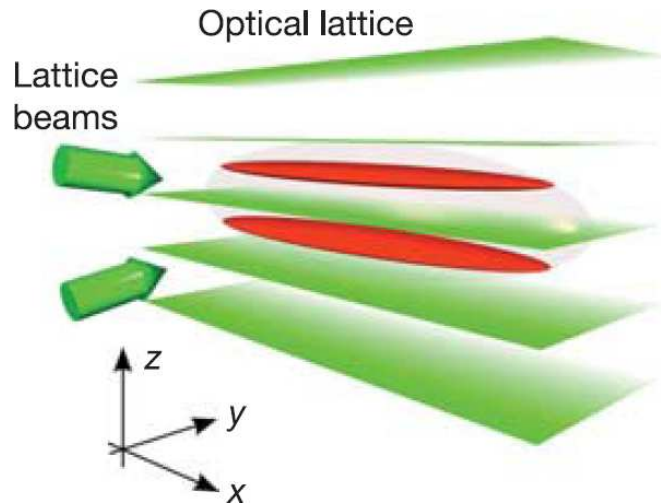


Figure 1.2: (Figure taken from Ref. [10]). An optical lattice is shown to divide a quantum degenerate 3D gas. The transparent ellipsoid represents the gas before applying the lattice and the red regions show two resulting 2D trapped gases after. The optical lattice is produced by two laser beams propagating in the y-z plane and intersecting at a small angle

the BKT phase. The first[17], reports the detection of phase defects in the interference of two or more 2D systems. The characteristics of these defects strongly imply the existence of free vortices. The second[10], demonstrates the algebraic decay of “off diagonal order”. The shift from algebraic to exponential decay of order was also shown to coincide with the proliferation of free vortices and was interpreted as the BKT transition (i.e. transition from normal to BKT phase). The third[12], shows the onset of bimodality as a critical atom number is surpassed, indicating a condensation of some variety. They claim, this critical atom number is of order 5 times higher than the ideal gas prediction for conventional Bose-Einstein condensation and suggest bimodality occurs at the same place the coherence properties change, i.e. at the BKT transition.

These results add support to the existence of a BKT phase, although, BEC has not yet been confirmed experimentally. The properties and boundaries of these phases are still far from clear.

## 1.4 Research Focus

The principle aim of this research is to investigate numerically, the behaviour of the proposed BKT phase transition, which occurs at  $T_{BKT}$ . Classical field simulations (CFS) applied to 2D ultra-cold Bose gases, lie at the core of this project. Specifically of interest, is whether a well defined phase transition occurs at all, and if so how this relates to the proposed microscopic BKT mechanism.

We focus on the behaviour of three macroscopic observables as the critical temperature  $T_{BKT}$  is traversed. These are, bimodality in the momentum distribution, the number and spatial location of vortices, and the position density distribution. The onset of bimodality infers the commencement of degeneracy. There is an emerging debate in the community as to the equivalence of bimodality with the BKT transition. We will use our methods to probe this relationship in detail.

The secondary focus, is to explore the self consistency of CFS, with a particular emphasis on the dependence of macroscopic parameters on the cutoff energy. Ideally, these parameters should not vary too much. Furthermore, we aim to find techniques that aid in the choice of initial parameters, for the production of desired equilibrium states.

## 1.5 Chapter Overview

In chapter 2, we further discuss 2D phases in the context of ultra-cold gases. Beginning with derivations for the ideal gas, we then focus on theoretical predictions for the trapped interacting regime, providing results for later comparison with simulations.

In chapter 3, we outline the motivation and numerical implementation of classical field simulations, followed by a discussion of the classical field energy cutoff.

In chapter 4, we present the main results of this research. That is, momentum bimodality, vortex distribution and peak position density, and the variation of these as the phase transition temperature  $T_{BKT}$  is crossed.

In chapter 5, we conclude, by summarising the results of our research and making comparisons with existing theory and experimental results.

In the appendix, we present results for the dependence of macroscopic parameters on the cutoff energy, and results of our attempt to develop techniques to aid in choosing initial state parameters.

# Chapter 2

## Phases of Two-Dimensional Bose Gases

In the first section of this chapter, we derive analytical predictions for the phases of 2D ideal gases. Some of these results are presented in convenient form for later comparison with our results in the interacting regime. Section two explores the (interacting) BKT phase transition in more depth, including an argument for the sudden onset of free vortices.

### 2.1 Ideal Gas Theory

For the ideal 2D Bose gas, information about the existence or behaviour of BEC can be gained from statistical mechanical arguments.

First, the density of states as a function of energy,  $g(\epsilon)$ , needs to be found. The requirement for BEC is that the density of states smoothly approaches zero as energy tends to zero. If BEC is possible then it will begin when the chemical potential  $\mu$  is significantly closer to the ground state energy  $\epsilon_0$ , than any other state[15].

By integrating  $g(\epsilon)$  multiplied by the Bose-Einstein distribution  $\bar{n}_{BE}$ , we obtain the number of atoms in the excited states

$$N_{ex} = \int_0^{\infty} g(\epsilon) \bar{n}_{BE} d\epsilon, \quad (2.1)$$

i.e. this result excludes the ground state occupation. If  $\mu$  is much less than  $\epsilon_0$ , then the occupation of the ground state is insignificant compared to the total number of bosons. Alternatively, if  $\mu$  is very close to  $\epsilon_0$ , then the ground state occupation is large and must be included in addition to  $N_{ex}$ . Hence, in both cases we take  $N_{ex}$  to represent the total number of bosons

in the excited states, refer to this as the thermal cloud. Then if the actual number of atoms in the system,  $N$ , exceeds  $N_{ex}(\mu = 0, T)$  (i.e. the saturated thermal cloud), the remaining atoms must reside in the condensate (ground state), i.e.  $N_{cond} = N - N_{ex}(\mu = 0, T)$ . Thus the condition for BEC is that  $N_{ex}(\mu = 0, T)$  is finite. Alternatively this can be inverted to give the more familiar critical temperature expression:  $T_c(N)$ , so that for  $N$  atoms, if  $T < T_c(N)$ , a finite condensate will exist.

In the next subsections we consider both the homogeneous and harmonically trapped cases.

### 2.1.1 Ideal Homogeneous Case

First, calculate the density of states for a 2D square with sides  $L$  (figure 2.1). Requiring the wavefunctions go to zero at the boundaries results in the modes being restricted to discrete energies  $\epsilon_n$  (equation 2.2).

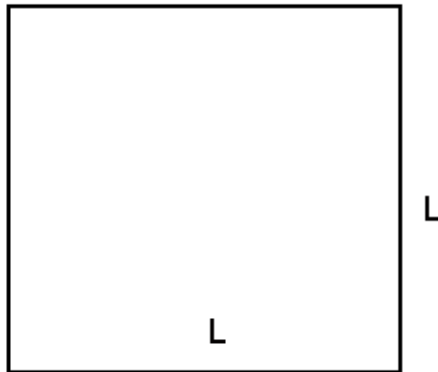


Figure 2.1:

$$\epsilon_n = \frac{h^2}{8mL^2}(n_x^2 + n_y^2) = \frac{h^2}{8mL^2}n^2, \quad (2.2)$$

where  $n_x$  and  $n_y$  are non-negative integers and

$$n^2 \equiv n_x^2 + n_y^2. \quad (2.3)$$

From figure 2.2 we can see the total number of states  $G(\epsilon)$  from  $n = 0$  to  $n = n_{max}$  is given by the area enclosed by the semicircle in the positive quadrant of  $n$ -space,

$$G(n_{max}) = \frac{1}{4}\pi n_{max}^2. \quad (2.4)$$

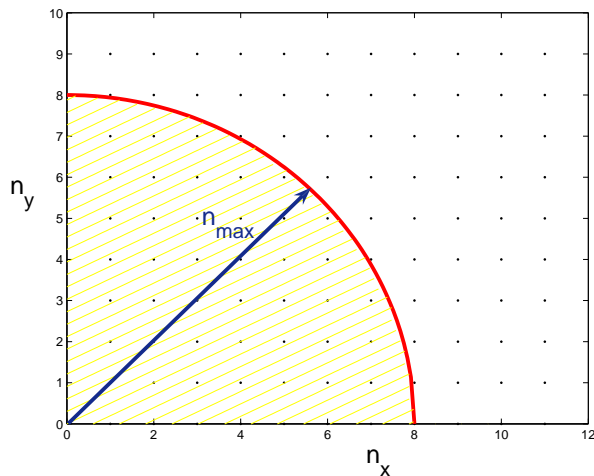


Figure 2.2:

Now, use equation 2.2 to write  $n_{max}$  in terms of  $\epsilon$ , then differentiate equation 2.4 with respect to energy to obtain the density of states

$$g(\epsilon) = \frac{2\pi mA}{h^2} \quad (2.5)$$

which notably is independent of  $\epsilon$ . This density of states does not go to zero, hence there is no BEC in the uniform case.

Recall,  $N_{ex}$  (equation 2.1) represents the total number of bosons in the excited states only. Plugging  $g(\epsilon)$  into this gives,

$$N_{ex} = \frac{2\pi mA}{h^2} \int_0^\infty \frac{1}{e^{\beta(\epsilon-\mu)} - 1} d\epsilon. \quad (2.6)$$

Multiplying both the top and bottom lines by  $e^{-\beta(\epsilon-\mu)}$  and changing variables to  $x = \beta(\epsilon - \mu)$  one obtains,

$$N_{ex} = A \frac{2\pi mkT}{h^2} \int_{-\beta\mu}^\infty \frac{e^{-x}}{1 - e^{-x}} dx = -A \frac{2\pi mkT}{h^2} \ln(1 - e^{\mu\beta}) \quad (2.7)$$

Crucially, as  $\mu \rightarrow 0$   $N_{ex}(\mu, T) \rightarrow \infty$ , which implies that the thermal cloud cannot be saturated, therefore BEC is not possible in the ideal homogeneous case.

### 2.1.2 Ideal Harmonically Confined Case

The energy states of a 2D harmonic oscillator are

$$\epsilon_n = \hbar(\omega_x n_x + \omega_y n_y), \quad (2.8)$$

where  $\omega_x$  and  $\omega_y$  are the trapping frequencies in the  $x$  and  $y$  directions respectively. For a given energy,  $\epsilon$ , the maximum quantum number in each direction are respectively

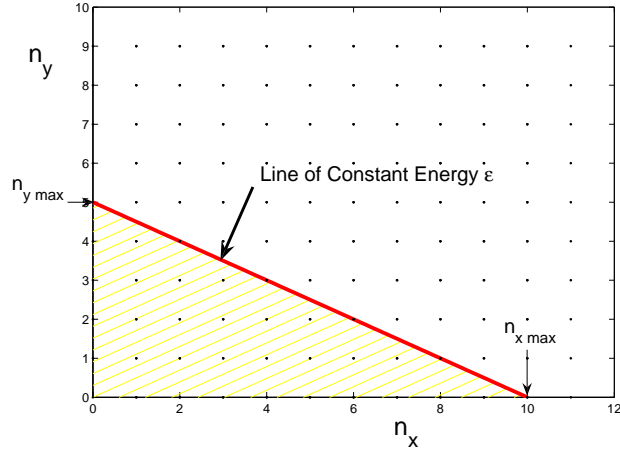


Figure 2.3:

$$n_{x \max} = \frac{\epsilon}{\hbar\omega_x}, \quad n_{y \max} = \frac{\epsilon}{\hbar\omega_y}. \quad (2.9)$$

The total number of states that have energy, from 0 to a given  $\epsilon$ , is represented by the area shaded in figure 2.3, i.e.

$$G(\epsilon) = \frac{1}{2}n_{x \max}n_{y \max} = \frac{\epsilon^2}{2\hbar^2\omega_x\omega_y}. \quad (2.10)$$

As done in the uniform case, we obtain the density of states by differentiating  $G(\epsilon)$  to get

$$g(\epsilon) = \frac{\epsilon}{(\hbar\bar{\omega})^2}, \quad \bar{\omega} \equiv \sqrt{\omega_x\omega_y}. \quad (2.11)$$

In contrast to the uniform case, this does go to zero proportionally to energy, hence a BEC will exist below critical temperature  $T_c$ . To find the critical temperature, apply equation 2.1, i.e.

$$N_{ex} = \int_0^\infty \frac{g(\epsilon)}{e^{\beta(\epsilon-\mu)} - 1} d\epsilon, \quad \beta \equiv \frac{1}{kT}, \quad (2.12)$$

where  $k$  is the Boltzmann constant and  $T$  is temperature. Changing variables to  $x = \beta(\epsilon - \mu)$  we obtain

$$N_{ex} = \left(\frac{kT}{\hbar\bar{\omega}}\right)^2 \int_0^\infty \frac{x}{e^x/e^{\beta\mu} - 1} dx \quad (2.13)$$

$$= \left(\frac{kT}{\hbar\bar{\omega}}\right)^2 \Gamma(2)g_2(e^{\beta\mu}), \quad (2.14)$$

$\Gamma$  is the gamma function and  $g_2$  is the Bose function (polylogarithm). Setting the chemical potential  $\mu$  equal to zero we get

$$g_2(1) = \zeta(2) = \frac{\pi^2}{6}, \quad (2.15)$$

$$\Gamma(2) = 1! = 1, \quad (2.16)$$

$$N_{ex}(\mu = 0, T) = \frac{\pi^2}{6} \left(\frac{kT}{\hbar\bar{\omega}}\right)^2, \quad (2.17)$$

where  $\zeta$  is the Riemann zeta function. Thus we obtain a finite saturated thermal cloud. Setting  $N_{ex} = N$  we can invert this to find the critical temperature  $T_c$ ,

$$T_c = \frac{\hbar\bar{\omega}}{k\pi} \sqrt{6N}. \quad (2.18)$$

Equation 2.14 shows the total number of bosons in the excited states, is proportional to  $T^2$ . Therefore, if  $N_{cond}$  is the number of bosons in the ground state then the condensate fraction is given by

$$\frac{N_{cond}}{N} = 1 - \left(\frac{T}{T_c}\right)^2. \quad (2.19)$$

Hence, for the trapped ideal gas, the condensate fraction versus temperature is an inverse parabola, as shown in figure 2.4.

### 2.1.3 Critical Density for Ideal Gas BEC

Here, we rephrase the condition for BEC in terms of the critical density instead of  $T_c$ . This turns out to be convenient for later comparison with results.

First, consider the ideal homogeneous case, equation 2.7 can be written as

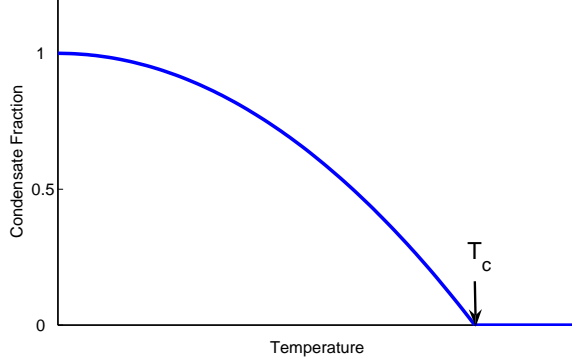


Figure 2.4:

$$N_{ex} = -\frac{A}{\lambda_{db}^2} \ln(1 - e^{\mu\beta}), \quad (2.20)$$

where

$$\lambda_{db} = \frac{h}{\sqrt{2\pi mkT}} \quad (2.21)$$

is the thermal deBroglie wavelength. Noting that  $N_{ex}/A$  is the the density per area,  $n$ , and rearranging this expression we arrive at the form,

$$n\lambda_{db}^2 = -\ln(1 - e^{\mu/(kT)}), \quad (2.22)$$

hence, as  $\mu \rightarrow 0$ ,  $n \rightarrow \infty$ , which is an alternative way of showing that the thermal cloud cannot be saturated and BEC is not possible in the 2D homogeneous case.

This should be contrasted to the ideal 3D homogenous case where the maximum density,  $n_c$ , is  $n_c\lambda_{db}^2 = 2.612$  [15]. Therefore in 3D, saturation of the thermal cloud is possible, resulting in BEC when  $N > N_{ex}(T)$ .

Focusing again on the ideal 2D trapped case, consider equation 2.14,

$$N_{ex} = \left(\frac{kT}{\hbar\bar{\omega}}\right)^2 \frac{\pi^2}{6} \quad (2.23)$$

This is finite, hence if  $N > N_{ex}(T)$ , the thermal cloud saturates with the excess atoms residing in the condensate. However, this condensate is a fragile phenomenon. To see this, use the local density approximation, which is to replace the chemical potential  $\mu$  by  $\mu + V(\mathbf{x})$  in equation 2.22, that is

$$n(\mathbf{x})\lambda_{db}^2 = -\ln(1 - e^{(\mu - V(\mathbf{x}))/(kT)}). \quad (2.24)$$

If this is integrated over all space the result reduces to equation 2.23. However since  $\mu = 0$ , this implies the density is infinite at the trap centre (where  $V(x) = 0$ ), even though  $N_{ex}$  is finite. Hence, the inclusion of any finite level of interactions would result in an infinite energy. The implications of this is that, even for very small interactions it is not clear from equation 2.23, whether BEC is possible in the interacting 2D trapped regime.

## 2.2 Berezinskii-Kosterlitz-Thouless Phase Transition

In the previous sections we have considered the ideal 2D gases, showing that BEC is only possible with a confining potential. Interaction effects are expected to greatly modify if not destroy these predictions.

### 2.2.1 Interacting 2D Trapped Regime

The interacting 2D trapped regime is very complicated as trapping effects compete with interaction effects. Much speculation has resulted and a prominent idea advocates the existence of 3 phases, this is described as follows. From cold to hot, these phases are BEC, BKT and thermal (or normal). We note, that the boundaries between these are by no means clear, there may also be considerable overlap. The termination of BEC occurs with the proliferation of paired vortices[16]. Paired vortices disrupt *off diagonal long range order*, resulting in algebraic decay and hence the BKT phase. BKT phase is disrupted with the swift appearance of free vortices, here superfluidity also ceases. As the temperature rises further, the increasing number of free vortices gradually destroys what remains of the BKT phase, producing the *quasi-condensate tail*.

For this research, we are primarily concerned with the BKT phase transition and the underlying proliferation of free vortices. Our results should help clarify the nature of the 2D trapped diagram.

### 2.2.2 Interacting 2D Homogeneous Regime

This subsection discusses the thermodynamics of free vortices at  $T_{BKT}$  for the homogeneous case, and their likelihood of appearing in the superfluid of the BKT phase[2]. The basic ideas of the homogeneous regime have been well understood since the 1970's, but the particular case of the 2D uniform Bose gas was only quantitatively analysed by Prokof'ev around the year 2000 using Monte Carlo methods.

Consider a free vortex centred in a disk of superfluid with radius  $R$ . The energy cost associated,  $E$ , is due to the kinetic energy of the superfluid,

$$E \propto \int_{\xi}^R v^2(r) r dr \propto \ln \left( \frac{R}{\xi} \right). \quad (2.25)$$

Where  $v(r) = \frac{\hbar}{mr}$  is the velocity field of a vortex as a function of radial distance  $r$  and  $\xi$  is the radius of the vortex core. Entropy,  $S$ , results as a consequence of positioning the vortex core of area  $\pi\xi^2$  in the superfluid disk of area  $\pi R^2$ .

$$S \propto \ln \left( \frac{R^2}{\xi^2} \right) \propto \ln \frac{R}{\xi}. \quad (2.26)$$

Because of the common factor of logs the Helmholtz free energy,  $F = E - TS$ , can be written in the form,

$$\frac{F}{kT} \approx (n_s \lambda_{db}^2 - 4), \quad (2.27)$$

where  $n_s$  is the superfluid density.

Plugging the free energy into the Boltzmann factor, predicts the likelihood of free vortices appearing in the superfluid. For a large system where  $R \gg \xi$ ,  $n_s \lambda^2 > 4$  results in a large positive  $F$  which implies free vortices are unlikely. Alternatively, if  $n_s \lambda^2 < 4$ ,  $F$  is large and negative indicating the proliferation of free vortices.

However, our simulation method (and experiments) measures total density,  $n$ , instead of  $n_s$ , hence of interest is how to relate these quantities. Prokof'ev et al. have investigated this in the case of weak, but realistic interactions, using quantum Monte-Carlo calculations[14]. For the critical total density,  $n_c$ , they obtain the following,

$$n_c \lambda_{db}^2 = \ln \left( \frac{\xi}{\bar{f}} \right), \quad (2.28)$$

where we have introduced the dimensionless interaction strength:

$$\bar{f} \simeq \sqrt{8\pi} \frac{a}{l_z} \ll 1, \quad (2.29)$$

with

$$l_z = \sqrt{\frac{\hbar}{m\omega_z}}. \quad (2.30)$$

The confinement scale,  $l_z$  is a function of particle mass,  $m$ , and the angular trap frequency in the tight direction,  $\omega_z$ . The scattering length is  $a$  and is a

measure of the collisional interactions between atoms, and the dimensionless number,  $\xi = 380 \pm 3$ , is numerically determined.

Equation 2.28 is of great interest to this project. Later, we will compare it with our harmonically trapped simulation results, to investigate whether or not this critical density is applicable to the harmonically trapped 2D gas.

### 2.2.3 Quasi-Condensate

In this dissertation we use the word condensate when broadly referring to any of BEC, BKT or quasi-condensate. This is convenient since our numerical method cannot directly decipher between these. Quasi-condensate is an important concept. Atoms in a quasi-condensate do not exhibit density fluctuations, just like a BEC, however the quasi-condensate does not have long range coherence that is characteristic of a BEC. It is likely that the BKT phase has properties of a quasi-condensate, although a *tail* of quasi-condensate may also extend to temperatures warmer than  $T_{BKT}$ . It is possible that bimodality is a characteristic of the quasi-condensate, as it is for BEC.

# Chapter 3

## Classical Field Simulations

### 3.1 Energy Modes and Phase Transitions

In the absence of interactions, the system modes are determined by the external potential. The trapping potential of interest here, is the 3D harmonic oscillator, which is sufficiently anisotropic to be quasi-2D in nature. The inclusion of interactions greatly modifies the states, such that a treatment in terms of single particle modes is impossible due to the nonlinear interactions between modes.

The low energy modes are spatially confined to the trap centre, and have relatively high occupation. The high energy modes, are more widely spread and their average occupation is comparatively low. Consequently, the centre of the trap is the region of greatest density.

The low energy modes are difficult to simulate because interactions are a significant parameter, due to their high density. The temperature range of primary interest is near the BKT critical temperature,  $T_{BKT}$ . However, a general property of phase transitions is strong fluctuations, in this case there are large density fluctuations in the system. These fluctuations mean that mean field theories are not appropriate for simulating the BKT regime.

### 3.2 Motivation

To model a bosonic gas by classical field simulations (CFS), the general idea is to divide the system modes into two regions (figure 3.1). The classical region contains the modes with energy below a cutoff  $E_{cut}$ , the incoherent region contains the remaining high energy modes above  $E_{cut}$ .

As discussed in §3.1, modes of the classical region exist predominantly in the trap centre where the density is high, thus interactions are dominant.

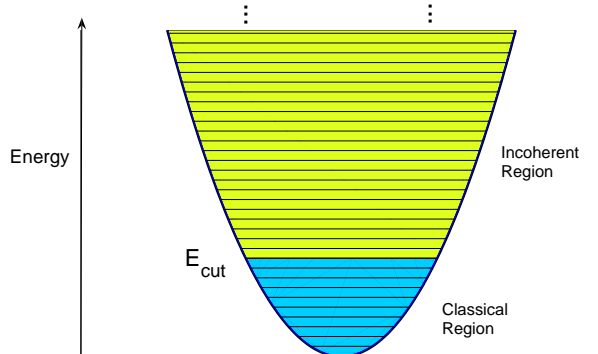


Figure 3.1: Partition of energy modes into two regions. The cutoff energy  $E_{cut}$  separates the incoherent from the classical region. Due to interactions, the physical energy states are vastly different to those shown at low energies

These strong interactions are difficult to model by traditional kinetic theories. However, the high mode occupation allows us to approximate these modes by classical fields [1]. For low occupations the classical field approximation is bad, as ultraviolet divergences occur. This is analogous to the ultra-violet catastrophe of Rayleigh-Jeans blackbody theory. For this reason the energy cutoff plays an important role in separating the highly occupied classical region from the sparsely occupied incoherent region.

For the low density incoherent region, interactions are relatively insignificant which makes modeling easier.

### 3.3 Classical Region Formalism

The following is a brief outline of the theory implemented numerically for inhomogeneous trapping potentials[1]. This theory is applicable to dilute Bose gases. For more general theory, see earlier work in references [3, 6, 7, 8].

The Hamiltonian  $\hat{H}$  can be described by that of the single particle  $\hat{H}_{sp}$  combined with the interaction Hamiltonian  $\hat{H}_I$  i.e.

$$\hat{H} = \hat{H}_{sp} + \hat{H}_I, \quad (3.1)$$

$$\hat{H}_{sp} = \int d^3\tilde{\mathbf{x}} \hat{\psi}^\dagger(\tilde{\mathbf{x}}) \left( -\frac{\hbar^2}{2m} \nabla^2 + V_{trap}(\tilde{\mathbf{x}}) \right) \hat{\psi}(\tilde{\mathbf{x}}), \quad (3.2)$$

$$\hat{H}_I = \frac{1}{2} U_0 \int d^3\tilde{\mathbf{x}} \hat{\psi}^\dagger(\tilde{\mathbf{x}}) \hat{\psi}^\dagger(\tilde{\mathbf{x}}) \hat{\psi}(\tilde{\mathbf{x}}) \hat{\psi}(\tilde{\mathbf{x}}), \quad (3.3)$$

where  $\hat{\psi}(\tilde{\mathbf{x}})$  is the quantum Bose field operator and  $\tilde{\mathbf{x}}$  is position. Interactions are approximated by the contact interaction strength  $U_0=4\pi\hbar^2 a/m$ , with  $a$  being the s-wave scattering length and  $m$  the atomic mass.

$V_{trap}(\tilde{\mathbf{x}})$  is the external harmonic trapping potential

$$V_{trap}(\tilde{\mathbf{x}}) = \frac{1}{2}m(\omega_x^2\tilde{x}^2 + \omega_y^2\tilde{y}^2 + \omega_z^2\tilde{z}^2), \quad (3.4)$$

where  $\omega_x$ ,  $\omega_y$  and  $\omega_z$  represent the angular frequencies of the trapping potential in the x, y and z directions respectively.

The field operator obeys the Heisenberg equation of motion

$$i\hbar\frac{\partial\hat{\psi}}{\partial t} = \left(-\frac{\hbar^2}{2m}\nabla^2 + V_{trap}(\tilde{\mathbf{x}})\right)\hat{\psi}(\tilde{\mathbf{x}}) + U_0\hat{\psi}^\dagger(\tilde{\mathbf{x}})\hat{\psi}(\tilde{\mathbf{x}})\hat{\psi}(\tilde{\mathbf{x}}). \quad (3.5)$$

However, this is unsolvable in our regimes of interest, unless further approximations are made. The general idea is to divide the field operator into a classical and incoherent region. This is done via projection, i.e.

$$\hat{\Psi}(\tilde{\mathbf{x}}) \equiv P\{\hat{\psi}(\tilde{\mathbf{x}})\} = \sum_{n \in C} \varphi_n(\tilde{\mathbf{x}}) \int d^3\tilde{\mathbf{x}}' \varphi_n^*(\tilde{\mathbf{x}}') \hat{\psi}(\tilde{\mathbf{x}}'), \quad (3.6)$$

$$\hat{\eta}(\tilde{\mathbf{x}}) \equiv Q\{\hat{\psi}(\tilde{\mathbf{x}})\} = \sum_{n \notin C} \varphi_n(\tilde{\mathbf{x}}) \int d^3\tilde{\mathbf{x}}' \varphi_n^*(\tilde{\mathbf{x}}') \hat{\psi}(\tilde{\mathbf{x}}'), \quad (3.7)$$

where  $C$  indicates the modes of the classical region and  $\varphi_n(\tilde{\mathbf{x}})$  denotes the eigenfunctions that diagonalise  $\hat{H}_{sp}$ . Hence  $\hat{\Psi}$  represents the classical field and  $\hat{\eta}$ , the incoherent field. The classical region is chosen such that it contains all the low energy modes below a cutoff  $E_{cut}$ . As explained in §3.2, it is important to choose  $E_{cut}$  such that modes in  $C$  are highly occupied, and the remaining modes of the incoherent region, sparsely occupied. Now, consider a system near equilibrium, where the average mode occupation decreases with increasing energy. If  $E_{cut}$  is chosen such that the average mode occupation at the cutoff, is of order 5, then the above condition should be satisfied.

The Heisenberg equation of motion can be split by applying projections 3.6 and 3.7. Now, consider only the classical part. The constituent modes are highly occupied, hence, we approximate the quantum field by a classical field, i.e.  $\hat{\Psi}(\tilde{\mathbf{x}}) \rightarrow \Psi(\tilde{\mathbf{x}})$ . Where  $\Psi(\tilde{\mathbf{x}})$  is a complex number, and is a function of  $\tilde{\mathbf{x}}$  and time. This is known as the classical field approximation. Mode occupation is no longer restricted to integer values. The final approximation is to neglect the effect of the incoherent modes, on the classical region. This is reasonable for two main reasons. The incoherent region has low density, thus does not significantly modify the effective potential experienced by classical

modes. Also, physical systems near equilibrium experience very little net flow of particles between classical and incoherent regions.

These approximations leave us with the projected Gross-Pitaevskii equation PGPE:

$$i\hbar \frac{\partial \Psi(\tilde{\mathbf{x}})}{\partial \tilde{t}} = \left( -\frac{\hbar^2}{2m} \nabla^2 + V_{trap}(\tilde{\mathbf{x}}) \right) \Psi(\tilde{\mathbf{x}}) + P\{U_0 |\Psi(\tilde{\mathbf{x}})|^2 \Psi(\tilde{\mathbf{x}})\}. \quad (3.8)$$

The projection operator  $P$  in the final term, retains the particles in the classical region, in the presence of s-wave collisions. The PGPE is the equation we implement numerically.

## 3.4 Numerical Implementation

### 3.4.1 Classical Region

For useful simulations, it is important that the modes below  $E_{cut}$  closely represent the physical system. Also, since all included modes are highly occupied, the propagation of every mode must be accurate.

To simplify the following notation, we take the harmonic trapping potential to be isotropic. Expressing the PGPE (3.8) in computational units (untilded), one obtains

$$i \frac{\partial \Psi}{\partial t} = -\nabla^2 \Psi + \frac{1}{4}(x^2 + y^2 + z^2) \Psi + C_{NL} |\Psi|^2 \Psi, \quad (3.9)$$

where we define units of distance  $x_0 = \sqrt{\hbar/2m\omega}$ , time  $t_0 = \omega^{-1}$  and energy  $\hbar\omega$ , where  $\omega$  is again the trapping frequency. For simplicity of describing the numerical implementation we have taken the harmonic potential to be isotropic. Also, define the nonlinear constant  $C_{NL} = N_C U_0 / \hbar\omega_z x_0^3$ . If the classical field  $\Psi$  is normalised to unity then  $N_C$  represents the number of bosons in the classical region.

The basis used to describe  $\Psi$  is that of the three-dimensional harmonic oscillator

$$\Psi(\mathbf{x}, t) = \sum_{\{l,m,n\} \in \mathcal{C}} c_{lmn}(t) \varphi_l(x) \varphi_m(y) \varphi_n(z), \quad (3.10)$$

where  $c_{lmn}(t)$  is the weighting and  $\{\varphi_n(x)\}$  are the eigenstate solutions of the one-dimensional harmonic oscillator. These states satisfy

$$\left[ -\frac{d^2}{dx^2} + \frac{1}{4}x^2 \right] \varphi_n(x) = \epsilon_n \varphi_n(x). \quad (3.11)$$

Noting,  $\epsilon_n = (n + \frac{1}{2})$  are the eigenvalues, and

$$\mathcal{C} = \{l, m, n : \epsilon_l + \epsilon_m + \epsilon_n \leq E_{cut}\}, \quad (3.12)$$

the PGPE can be written as

$$\frac{\partial c_{lmn}}{\partial t} = -i[(\epsilon_l + \epsilon_m + \epsilon_n)c_{lmn} + C_{NL}F_{lmn}(\Psi)]. \quad (3.13)$$

In deriving this expression, we have made use of the fact that the harmonic oscillator states are orthogonal. The matrix element of the nonlinear term

$$F_{lmn}(\Psi) \equiv \int d^3\mathbf{x} \varphi_l^*(x) \varphi_m^*(y) \varphi_n^*(z) |\Psi(\mathbf{x}, t)|^2 \Psi(\mathbf{x}, t), \quad (3.14)$$

can be evaluated exactly, by selecting an appropriate Gauss-Hermite quadrature.

The PGPE (3.13) is now in a form that can be implemented numerically. One of the key features of CFS, is that it accounts for fluctuations such as vortices, which is essential to accurately describe finite temperature 2D gases.

### 3.4.2 Incoherent Region

Modeling the incoherent region is comparatively simple. Final temperature, chemical potential  $\mu$  and density of the classical region  $n_{below}$  are calculated before we analyse the incoherent region, and are taken as inputs. Using these parameters, Hartree-Fock theory is implemented, similar to that used in ref. [9].

The density of the above region,  $n_{above}(x, y)$ , is calculated by the semi-classical integration of the Bose-Einstein distribution over momentum components,  $p_x, p_y$ ,

$$n_{above}(x, y) = \frac{1}{h^2} \iint_{\mathcal{T}} dp_x dp_y \frac{1}{e^{\beta(E_{HF}(x, y, p_x, p_y) - \mu)} - 1}, \quad (3.15)$$

where,

$$E_{HF}(x, y, p_x, p_y) = \frac{p_x^2 + p_y^2}{2m} + V_{trap}(x, y, z = 0) + \frac{1}{2} \hbar \omega_z + 2 \frac{\hbar^2}{m} \tilde{g} (n_{below}(x, y) + n_{above}(x, y)) \quad (3.16)$$

is the Hartree-Fock approximation to the energy.  $V_{trap}$  is the harmonic potential and  $\omega_z$  is the trapping frequency in the tight direction. Interactions enter this expression via  $\tilde{f}$ ,

$$\tilde{f} = 4\pi a \int_{-\infty}^{\infty} dz |\phi_0(z)|^4, \quad (3.17)$$

$a$  is again the scattering length and  $\phi_0(z)$  is the solution to the harmonic oscillator wave function, in the  $z$ -direction. The region of integration,  $\tau$ , is given by

$$\left( \tau : \left\{ \frac{p_x^2 + p_y^2}{2m} + V_{trap}(x, y, z = 0) + \frac{1}{2}\hbar\omega_z \geq E_{cut} \right\} \right), \quad (3.18)$$

which is the incoherent region. On the right hand side of equation 3.15, the density of the classical region,  $n_{below}$ , is calculated from CFS, while that of the incoherent region,  $n_{above}$ , is originally taken to be zero. The resulting  $n_{above}$  is iteratively substituted into the right hand side until  $n_{above}$  does not change. This is known as self-consistent Hartree-Fock theory.

We now know the total density  $n = n_{above} = n_{below}$ , and hence the total number of atoms.

## 3.5 Simulation Procedure

### 3.5.1 Macroscopic Parameters

Some macroscopic parameters are conserved under classical field evolution, while others, not. The constant parameters of interest are, the number of (classical region) particles and total energy of the classical region, and are input parameters to the calculations. Other parameters are determined from the results of a simulation by appropriate averages, e.g. temperature is calculated via a scheme that generalises Rugh's dynamical definition of temperature [5, 4]. This scheme is nonperturbative and quite accurate. Following work by Penrose and Onsager [13], the condensation fraction is calculated by the one-body density matrix

$$\rho_C(\mathbf{x}, \mathbf{x}') \equiv \langle \hat{\psi}^\dagger(\mathbf{x})\hat{\psi}(\mathbf{x}') \rangle_{ensemble}. \quad (3.19)$$

This is a measure of phase coherence across space. Greater coherence is associated with a larger condensation fraction.

### 3.5.2 Procedure

For the purposes of this project we are only interested in equilibrium states. The general idea is to choose a random initial state (but of known energy and  $n_{below}$ , followed by time evolution until equilibrium is reached. Finally, the state of the incoherent region is calculated to match the temperature and chemical potential of the classical region, then we obtain the total density and number of atoms in the full system.

Understanding how equilibrium is reached can be gained from the ergodic hypothesis. First, recall the *fundamental assumption of statistical mechanics*, that all accessible microstates of an isolated system, are equally probable. By definition, the most probable macrostates are equilibrium states. Hence, the question of reaching equilibrium reduces to the question of whether time evolution allows the exploration of a large number of microstates. Mode mixing due to nonlinear interactions, provides the mechanism for exploring microstates. Thus, under evolution this system appears to be ergodic.

In the classical region, an initial state can be chosen with the desired constants of motion mentioned in §3.5.1. However, the current scheme does not allow direct control of temperature, condensate fraction or number of particles in the incoherent region. Hence, we do not directly control the total number of particles either.

After reaching equilibrium, the state of the classical region is allowed to evolve further. Many equilibrium states are then used to obtain averages for temperature, chemical potential and density distribution. These parameters are then used to calculate the state of the incoherent region, see §3.4.2. Combining the classical and incoherent regions, produces the equilibrium information for the full (i.e. classical + incoherent) harmonically trapped Bose gas.

### 3.5.3 Cutoff Energy

An important question to consider is, what values of  $E_{cut}$  are acceptable for a given system? The least occupied (average occupation) mode of the classical region, is a parameter of great interest, which we denote as  $n_{min}$ . Understanding this comes from the Bose-Einstein distribution for average mode occupation

$$\bar{n}_{BE} = \frac{1}{e^{(\epsilon-\mu)/kT} - 1}, \quad (3.20)$$

thus, mode occupation decreases as mode energy increases. The validity requirement for CFS is that  $n_{min} \gtrsim 1$ . Alternatively, if  $n_{min}$  is too large then this implies highly occupied modes are being described by Hartree-Fock theory which does not take into account fluctuations such as vortices. The choice of cutoff energy is determined by the iterative procedure of running the simulation, evaluating  $n_{min}$  then readjusting  $E_{cut}$ .

### 3.5.4 Simulation Modes

Comparing the shape of the curves in figure 3.2, shows that interactions cause spatial *spreading* of the ground state wavefunction, in this case by a factor of

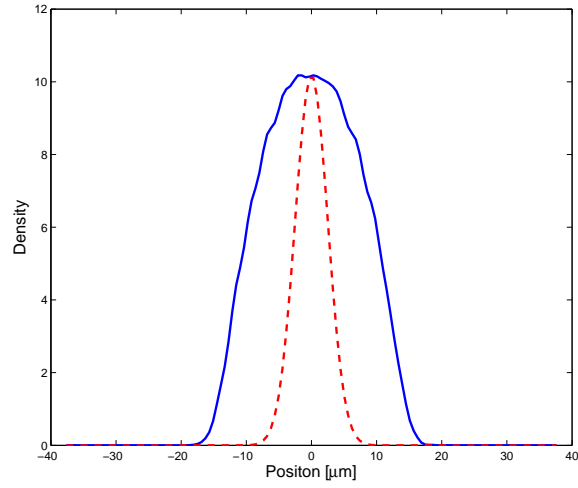


Figure 3.2: The solid blue line is a 1D slice of a typical condensate wavefunction produced by CFS. The red dashed line is the gaussian ground state for the same trap parameters but without interactions. Note, the gaussian is not normalised

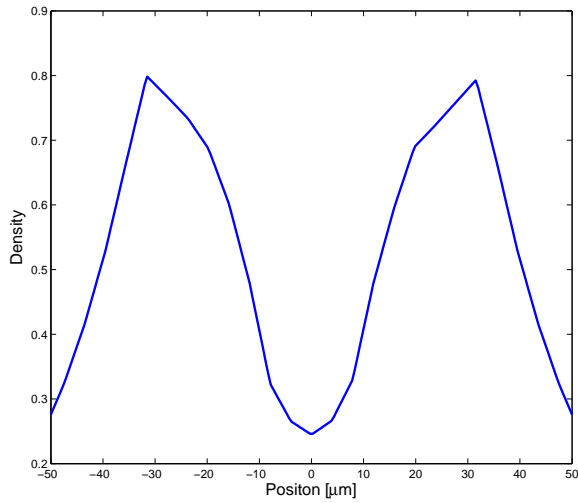


Figure 3.3: Here is a typical density slice of the incoherent region only, produced by our simulations.

order 3. This is qualitatively in agreement with the discussion of §3.1. Figure 3.3 shows the combination of all modes in the incoherent region. Note the

incoherent density is  $\sim 10$  times less than the condensate.

### **3.6 CFS Summary**

Importantly, the methodology elucidated in this chapter is only applicable to nonzero temperatures. That is, it applies to systems that have substantial excited state populations. This is due to the requirement of accurately separating the highly occupied classical region from the sparsely occupied incoherent region. Also, CFS include the modeling of density fluctuations such as vortices, which is necessary to model 2D Bose gases. Hence, CFS provide a very useful tool for theoretically investigating the BKT phase.

# Chapter 4

## Phase Results

### 4.1 Results for Experimental Trap Parameters

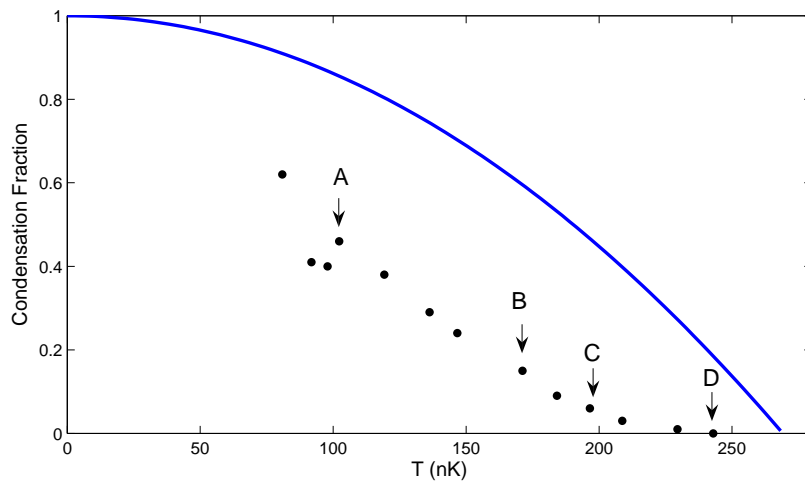


Figure 4.1: The black dots represent the condensation fraction for simulations of different temperature, while keeping the total number of atoms fixed at approximately 44000. The solid blue line is the ideal gas prediction calculated using equation 2.19.

Here we present simulation results for the experimental trap parameters utilised by the ENS group[12]. The trap confinement frequencies in the x, y and z directions are 9.4, 125 and 3000 Hz respectively. Rubidium atoms were used and the dimensionless interaction strength,  $\tilde{f}$ , was 0.13.

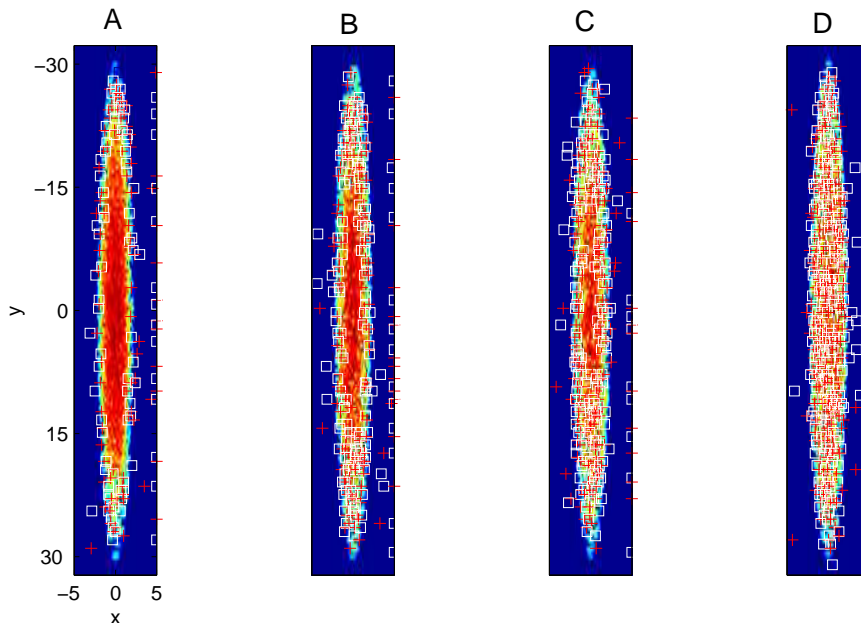


Figure 4.2: These are typical position density plots for the classical region. The position axis are the loose directions,  $x$ ,  $y$ , and are in units of  $\mu m$ . The density has been integrated over the tight direction,  $z$ , and the  $\log_{10}$  has been taken. Red indicates the greatest density and blue represents the least. Each plot has been labeled a letter which relates to the corresponding letter in figure 4.1. Vortices of opposite circulations are represented by  $\square$  and  $+$ .

Figure 4.1 shows that the condensation (quasi-condensation) is shifted downward significantly compared with the ideal gas prediction due to interactions. In figure 4.2 we show typical density profiles at various temperatures. We note the elongated shape of the gas due to trapping anisotropy in the loose directions. These plots are of the classical region only, the incoherent region is less interesting because of the low density. Comparing figures 4.2 and 4.1 we see that from simulation A to D, the temperature increases by approximately 150 nK and the condensate fraction decreases from 0.46 to approximately zero. As the temperature rises, vortices encroach deeper into the trap centre which coincides with the loss of condensate.

Approximately 100 additional simulations were performed beforehand to find equilibrium states with the required total number of atoms and an acceptable  $E_{cut}$ , for the wide range of temperatures we have in these plots. Each simulation in this regime took approximately 24 hours, hence by using multiple processors, these results took over two months to obtain. Because

of time restraints, we decided to abandon this regime in favour of a trap parameters that allowed simulations of duration between 1 and 4 hours and the remainder of this chapter is concerned with these results.

## 4.2 Characterisation of BKT Transition

For the interacting 2D trapped regime, it has been claimed[12] that the BKT transition coincides with,

- (1) the onset of bimodality,
- (2) the attainment of a critical peak density,  $n_{peak}^c$ , that was predicted by uniform Bose gas Monte Carlo calculations to obey the following,

$$n_{peak}^c \lambda_{db}^2 \approx \ln \left( \frac{\xi}{\bar{f}} \right). \quad (4.1)$$

The left hand side of this equation is of the same form as the equation 2.28 derived earlier for the interacting homogenous case, however, the right hand side is a universal form that depends solely on interactions through  $\bar{f}$ . They claim that by using peak density, the equation also applies to the trapped system. One of the aims of this chapter is to investigate the validity of these two claims, the other, is to characterise the behaviour of vortices as we cross the BKT transition. To better understand the physics we measure the temperatures where properties (1) and (2) are observed in our simulations. We define  $T^{(1)}$  to be the temperature at which bimodality begins, and  $T^{(2)}$  to be the temperature for which the predicted peak density is reached. We also introduce a third temperature,  $T^{(3)}$ , which is an estimate of  $T_{BKT}$  from considering the shape of the condensate fraction versus temperature curve.

### 4.2.1 Parameters

We explore the BKT transition in four different regimes. All systems have isotropic loose directions with the trapping frequency 9.4 Hz. Two systems have tight direction confinement (a),  $f_z = 940$  Hz and the other two have (b)  $f_z = 1880$  Hz, these correspond to (a)  $\bar{f} = 0.075$  and (b)  $\bar{f} = 0.107$  for  $^{87}\text{Rb}$  atoms. We have taken the mass of  $^{87}\text{Rb}$  to be 86.9 atomic mass units and the scattering length as 5.29 nm. For each of these two trap configurations, the number of atoms in the classical region is varied, which has the effect of modifying the temperature at which condensation occurs. The details of parameters for each regime are listed in table 4.1,  $C_{NL}$  is the nonlinear

Table 4.1:

<i>Regime</i>	$f_z$	$C_{NL}$	$E_{cut}$	$f$
A	940	300	80	0.075
B	940	600	95	0.075
C	1880	200	125	0.107
D	1880	300	130	0.107

constant appearing in by equation 3.13, and is proportional to the number of atoms in the classical region.

All simulations for the four regimes proceeded in a similar manner. First, a few *pilot* simulations were performed to find parameters that bound the region where the condensate fraction varies from  $\lesssim 50\%$  down to  $\sim 1\%$ . We expect the BKT transition will occur in this region. The cutoff energy was taken into consideration and chosen such that, near the transition point,  $n_{min}$  remained within the range 4 to 6. Next, while holding all over parameters constant, the energy was varied such that different points across the BKT transition were simulated. We note that because energy is the only variable, the total number of atoms is not constant, and ranged between approximately  $5 \times 10^3$  and  $5 \times 10^4$ . Note: this is because while we keep the classical region population (i.e.  $C_{NL}$ ) fixed, as the temperature (energy) increases the incoherent region is populated with an increasing number of atoms. For each regime approximately 200 simulations were run. This took more than 3 weeks of computer time on a multiprocessor machine and involved large amounts of data analysis and organisation.

## 4.2.2 Bimodality in Momentum Distribution

The first question to address, is how to measure the temperature,  $T^{(1)}$ , at which bimodality begins in the momentum distribution. Extensive averaging is required because we are near a critical point with strong fluctuations, this is particularly necessary to obtain smooth momentum and position density distributions. For the results of each simulation, 2 thousand equilibrium states, and both the  $x$  and  $y$  directions were used for averaging, which was possible because of the symmetry of the traps in these directions. A 3D plot combines the distribution produced by each simulation as a function of the equilibrium temperature. These distributions were then binned according to temperature, with each bin containing approximately 4 simulations, for example see figures 4.3 and 4.4, which summarise our results for 2 parameter regimes.

Bimodality occurs when the occupation of the condensate/quasi-condensate

number becomes a significant fraction of the total atom number. The quasi-condensate density profile, which is almost Gaussian, then becomes a prominent feature of the momentum distribution, amongst the background of many lowly occupied excited states. Thus, bimodality presents itself as a “*bump*” in the momentum distribution.

From these plots, figures 4.3 and 4.4, we note that bimodality has a gradual onset and identifying the exact point is difficult. The method used here, is to note the base of the prominent mode, forms an elongated crescent shape. The elbow of this crescent, which is at the high temperature end, is taken to be where bimodality begins, and the simulation at this temperature is drawn with a thick red line. Most error arising from this method, is due to the possibility of “*weak*” bimodality at higher temperatures not being detectable to the eye. For this reason, the error bar extends 3 nK in the cold direction but 13 nK in the hot direction. Hence, the red line best represents the lower bound for temperature at the onset of bimodality. The critical temperatures,  $T^{(1)}$ , for the onset of bimodality in the different regimes are summarised in table 4.2. An important observation is, the onset of bimodality is gradual, though it rapidly accumulates beyond  $T^{(1)}$ , which would be most obvious in experiments with limited resolution.

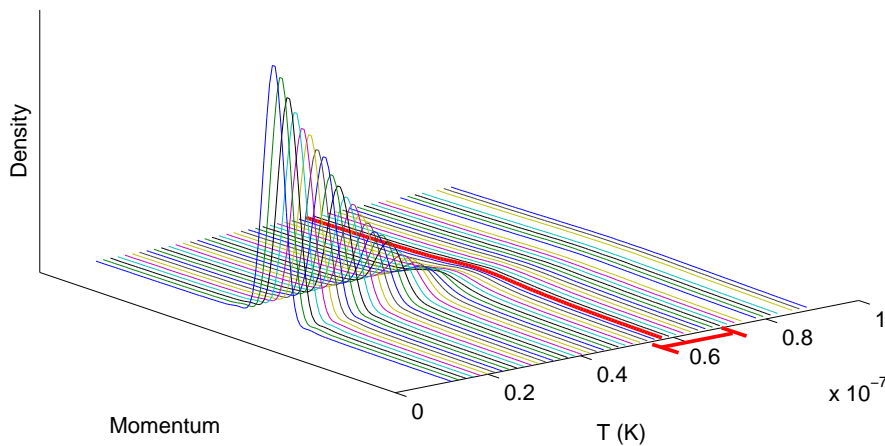


Figure 4.3: Regime D: The thick red line represents the simulation at the onset of bimodality. The red line parallel to the temperature axis represents the error bar for critical temperature  $T^{(1)}$ .  $C = 300$ ,  $f_z = 1880$  Hz,  $E_{cut} = 130$

From figures 4.3 and 4.4 we can see that the general shape of these mo-

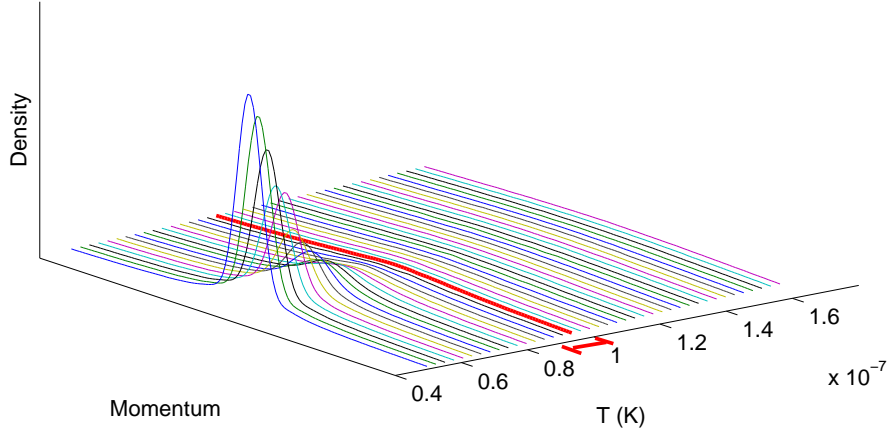


Figure 4.4: Regime B:  $C = 600, f_z = 940 \text{ Hz}, E_{cut} = 95$

Table 4.2:

<i>Regime</i>	$T^{(1)}(nK)$
A	69
B	93
C	53
D	58

momentum distributions are similar. The different values of  $T^{(1)}$  are due to the different strengths of confinement in the tight direction, characterised by  $f_z$ , and the different number of atoms in the classical region. We note that the plot of regime D extends to colder temperatures than regime B.

### 4.2.3 Peak Density in Position Space

In this section we note the behaviour of the position density of as a function of  $T$ , and importantly address the issue of how to relate the critical density, discussed in §4.2, to our simulation results.

The position density distribution of regime D (figure 4.5) has a number of interesting features. From cold to warm, the position distribution spreads out, as the fraction of atoms in higher energy modes increases. The area under each curve is proportional to the total number of atoms in that system. It can be seen that this number does not change significantly from zero

temperature to about 40 nK, beyond here the number rises sharply. This region of relatively constant number is due to the population of the classical region being fixed, and the occupation of the incoherent region modes being negligible.

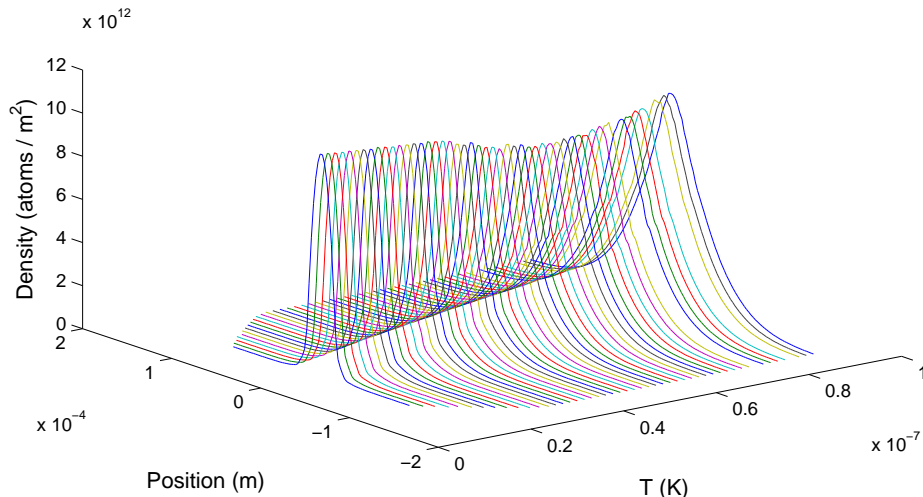


Figure 4.5: Regime D: A typical position distribution as a function of temperature as the BKT transition is crossed.  $f_z = 1880$  Hz.

Now we focus on finding the temperature at which the predicted peak critical density,  $n_{peak}^c$ , occurs (equation 4.1). For regime D,  $\bar{f} = 0.107$ , and  $n_{peak}^c \lambda_{db}^2 = 8.18$ . In figure 4.6, the position values of the distribution (figure 4.5) are multiplied by the deBroglie wavelength  $(\lambda_{db})^2$ , which is a function of temperature. Only the peak values, which comprise the central ridge, are of interest, these are plotted in figure 4.7 for regime D.  $n \lambda_{db}^2$  is a characterisation of degeneracy. Interestingly, while the peak density does not change much with  $T$  (see figure 4.5), the degeneracy changes much more significantly (see figure 4.6). As shown, these plots are used to find the temperature,  $T^{(2)}$ , at which  $n_{peak}$  satisfies 4.1, the results summarising our 4 regimes are displayed in table 4.3.

#### 4.2.4 Condensation Fraction versus Temperature

Here we bring together the results of the previous subsections by comparing  $T^{(1)}$  and  $T^{(2)}$  on plots of condensate fraction versus temperature (figures 4.8, 4.9, 4.10, 4.11). It is important to point out that the numerical method

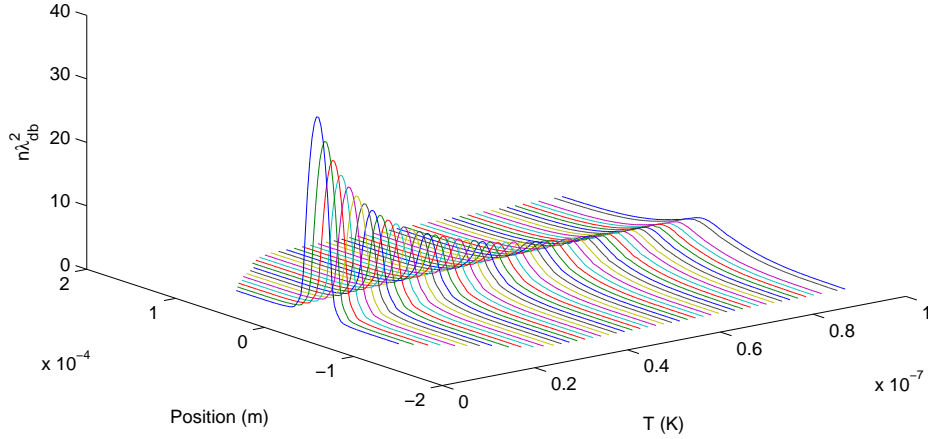


Figure 4.6: Regime D: The same data as for figure 4.5, except the points of each curve have been multiplied by the deBroglie wavelength squared.

Table 4.3:

<i>Regime</i>	$T^{(2)}(nK)$
A	47.3
B	65.3
C	33.4
D	42.2

does not decipher between BEC or BKT, and a finite condensate fraction can be equally well identified as a quasi-condensate rather than a pure condensate.  $T^{(1)}$  and  $T^{(2)}$  are also compared with  $T^{(3)}$ , which is calculated by aligning a tangent to the condensate curve and finding the intercept with the temperature axis. This is a crude approximation for graphically finding the degeneracy temperature, and the large error bars indicate the uncertainty of identifying key features. We were motivated to define this temperature because of the peculiar condensation fraction versus temperature shape, which was common to all our results.

We note, the transition temperature for regime A is of order 25 nK cooler than that for B, even though they have the same trapping parameters. This difference is due to regime A having, of order, half as many atoms as B, hence to reach the required degeneracy for condensation, regime A needs to be cooler. A further examples is illustrated by regime C having a critical

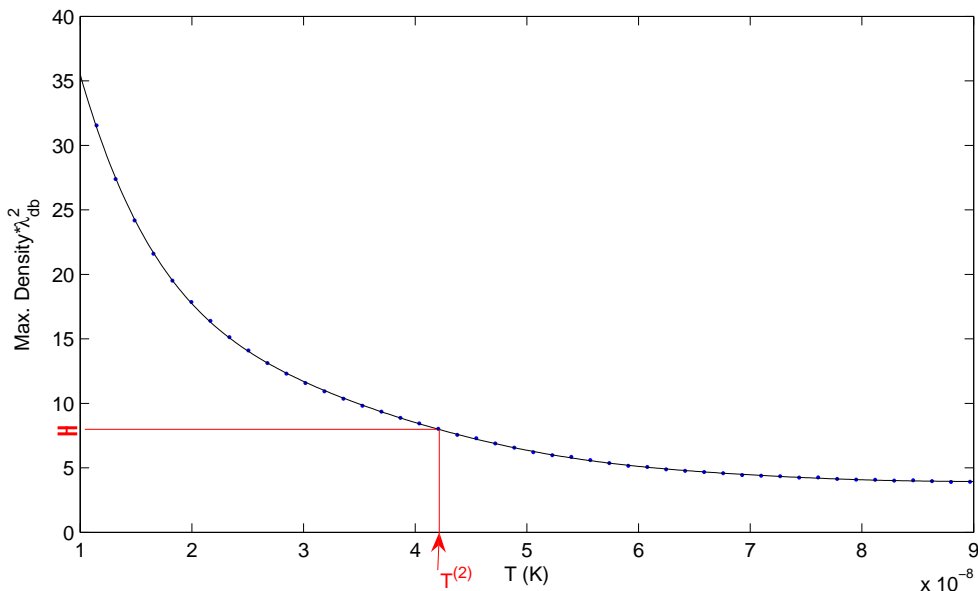


Figure 4.7: Regime D: The maximum density of each curve of figure 4.6. The fitted curve is used to aid finding the values of  $T^{(2)}$  for a given maximum density, the error for this step is small as indicated by the red error bar on the y-axis.

temperature approximately 9 nK cooler than D, where C has of order 50 percent fewer atoms.

However, the most important features of figures 4.8, 4.9, 4.10 and 4.11 is the relationship between  $T^{(1)}$ ,  $T^{(2)}$  and  $T^{(3)}$  within each graph alone. In each regime, the temperature at the onset of bimodality,  $T^{(1)}$ , occurs when the condensation fraction reaches between 0.2 and 2.5 percent. The method we use for detecting bimodality should only be sensitive to a difference at least of order 1 percent. This implies the onset of bimodality and condensate/quasicondensate occur at the same temperature.

Now, consider the temperature at the critical maximum density,  $T^{(2)}$ , predicted by equation 4.1. These all occur at similar positions relative to the shape of the condensation curves (where the condensate fraction begins to increase rapidly), which is reflected by the agreement of  $T^{(2)}$  with  $T^{(3)}$ , to within at least 6 nK. This is remarkable when taking into account the parameter differences between regimes. The total number of particles, tight direction trapping potential and critical temperature vary by a factor of order 2 between the different regimes, yet still  $T^{(2)}$  provides a relatively consistent prediction of the critical temperature.

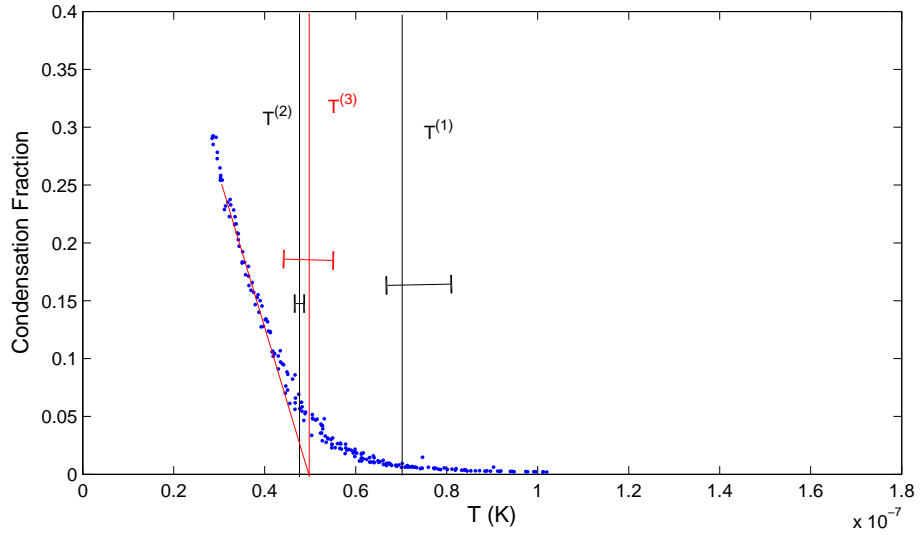


Figure 4.8: Regime A: This curve shows how the condensation fraction behaves as a function of temperature. The slanted line is the tangent of the curve when the condensation fraction is 0.2, this is our method for estimating  $T^{(3)}$ .  $T^{(1)}$ ,  $T^{(2)}$  and  $T^{(3)}$  are represented by vertical lines with corresponding error bars drawn at the centre.  $f_z = 940$  Hz.

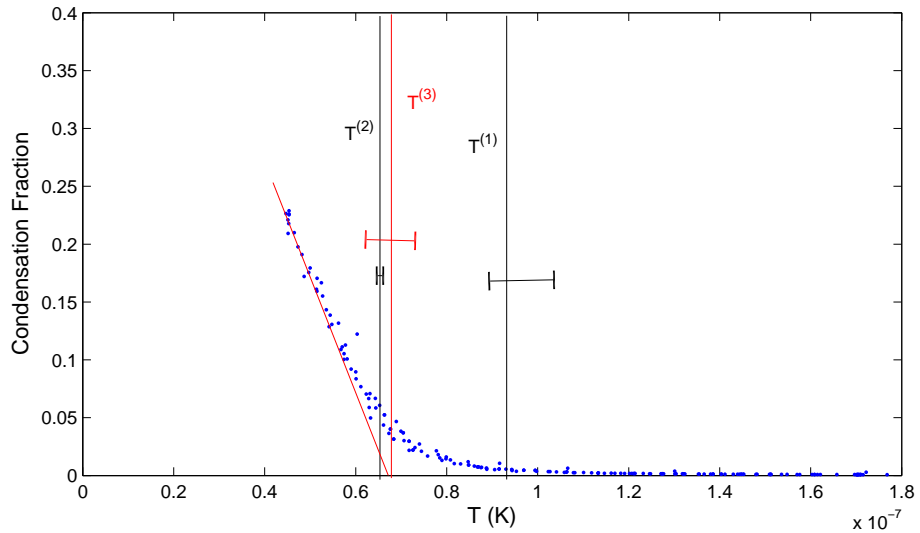


Figure 4.9: Regime B:  $f_z = 940$  Hz.

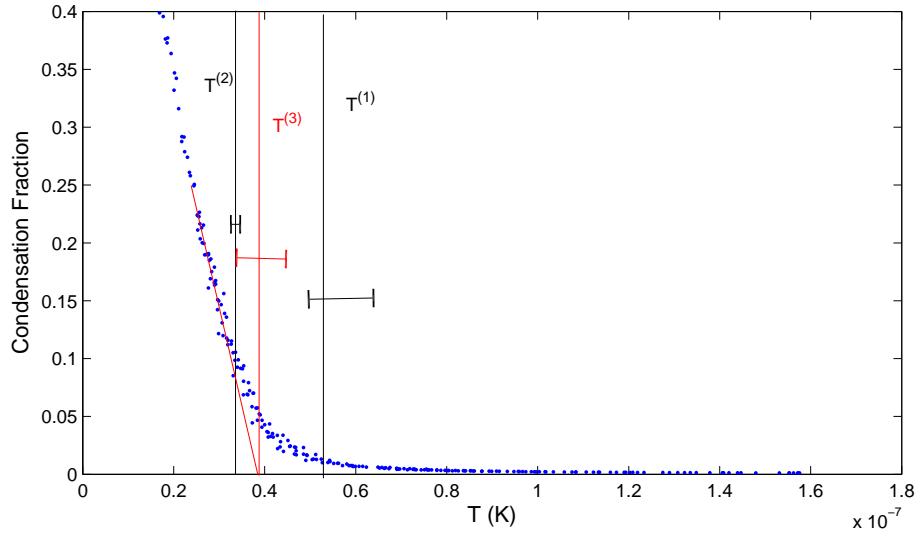


Figure 4.10: Regime C:  $f_z = 1880$  Hz.

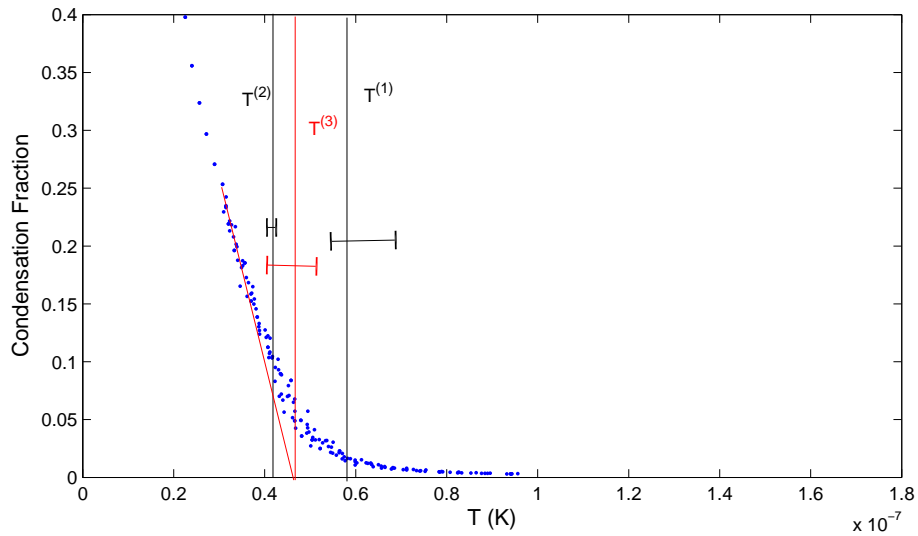


Figure 4.11: Regime D:  $f_z = 1880$  Hz.

When comparing  $T^{(1)}$  with  $T^{(2)}$ , these results consistently show that the onset of bimodality occurs at higher temperatures than the transition temperature predicted by equation 4.1, to well within our errors. More specifically, bimodality begins, on average, 21 nK warmer than  $T^{(2)}$ . Effectively for these results, this is a lower bound to the discrepancy, since bimodality may begin

at warmer temperatures where it is difficult to detect by our method. The consistent discrepancy between  $T^{(1)}$ ,  $T^{(2)}$  is in disagreement with the claim proposed by reference [12], which are suggesting both are the same. To find where the BKT transition occurs relative to the temperatures defined in this sections requires further investigation, and a direct measure of superfluidity which we do not have.

### 4.2.5 Phase Diagrams

Here we propose combining the results of the last subsections into thermal  $N$ - $T$ , phase diagrams (figures 4.12, 4.13). The red curves represent the phase boundaries, these we predict to pass through zero since the critical temperature must decrease with total number to preserve the required critical density of equation 4.1. The shape of these phase boundaries is not intended to be an accurate description, since there are only 2 data points per curve. More regimes for a fixed value of  $\bar{f}$ , must be investigated for a precise description of shape.

These phase diagrams give a picture of the normal phase, and the band of quasi-condensate joining onto the BKT phase. The BKT phase is likely further divided into a BEC phase at low temperature, but we have not identified this phase here. The BKT transition is a well-known “higher order” transition, surrounded by a large fluctuation region. The  $T^{(1)}$  - quasi-condensate transition signifies the onset of this fluctuating region leading up to the BKT transition.

### 4.2.6 Vortices in Position Space

In the following figures 4.14 to 4.17 we show typical instantaneous density plots for regime D as the temperatures is varied, such that the condensate fraction decreases from 0.59 to 0.008. Vortices are shown by  $\square$  and  $+$ , with the different symbols indicating opposite circulations. Figure 4.14 shows the spatial distribution well below  $T^{(2)}$ , the condensate is quite stable and is confined to the trap centre (shown red), with vortices banished to the outer edges. Figure 4.15 shows a gas with  $T < T^{(2)}$ , the vortices are paired but suppressed from the centre. Figure 4.16 is for a region with  $T^{(2)} < T < T^{(1)}$ , vortices exist throughout but appear to be paired (i.e.  $\square$  and  $+$  are close to each other). Finally, figure 4.17 represents a region with  $T > T^{(1)}$ , there are many vortices throughout the trap and pairing is no longer clear. It appears that there are many broken pairs or at least well separated pairs.

We have further observed there is a tendency for vortex pairs to align with each other, analogous to the behaviour of electric dipoles.

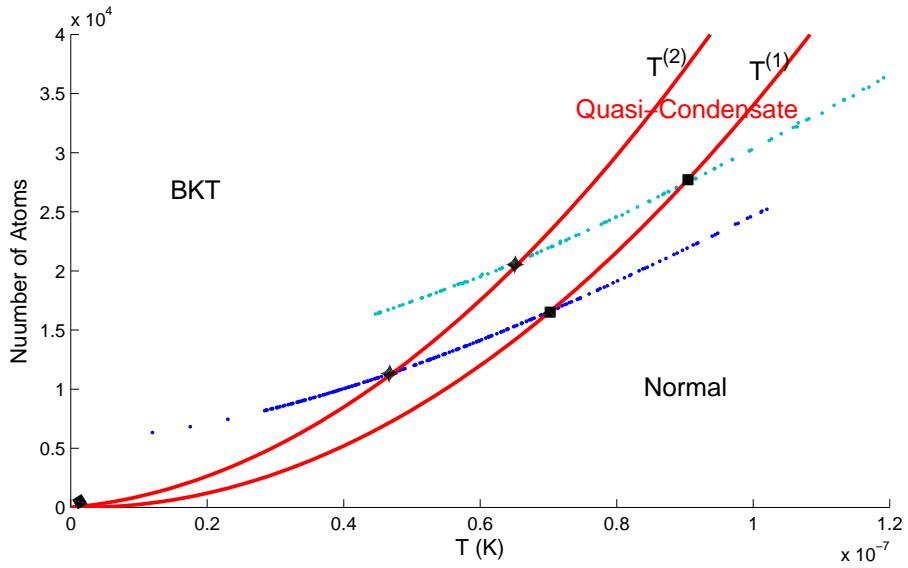


Figure 4.12: Phase diagram showing BKT, quasi-condensate and normal (thermal) (note: BEC not considered). The upper blue curve represents regime B and the lower represents regime A. The red lines cross these curves at points  $T^{(1)}$  and  $T^{(2)}$ .  $f_z = 940$  Hz.

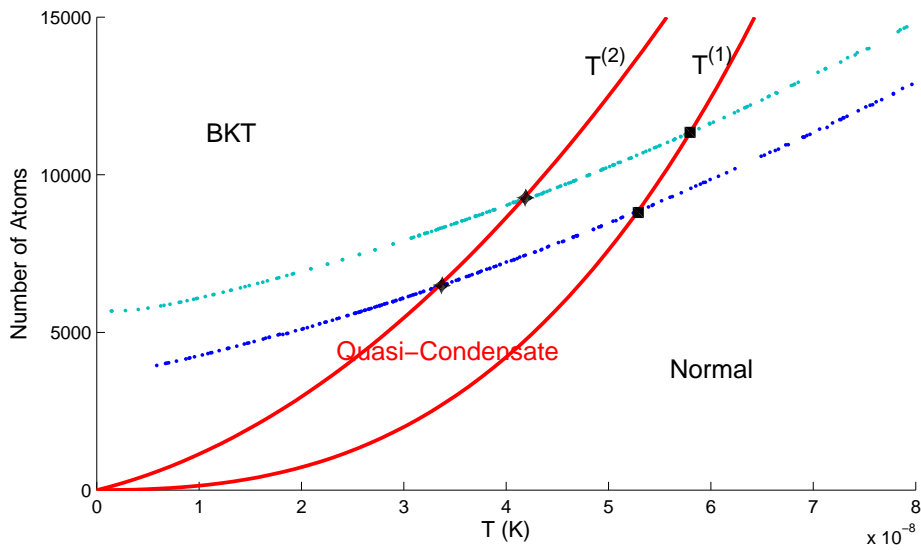


Figure 4.13: Regime C and D:  $f_z = 1880$  Hz.

We note that to some degree, the proximity of  $\square$  and  $+$  is due to the

vortex creation mechanism which conserves angular momentum. In the next subsection we present findings that show pairing is promoted by at least another mechanism.

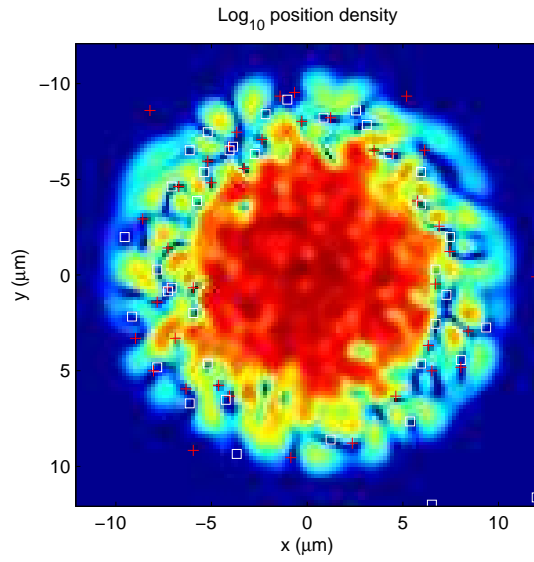


Figure 4.14: Regime D:  $T = 14.5$  nK, condensate fraction = 0.59

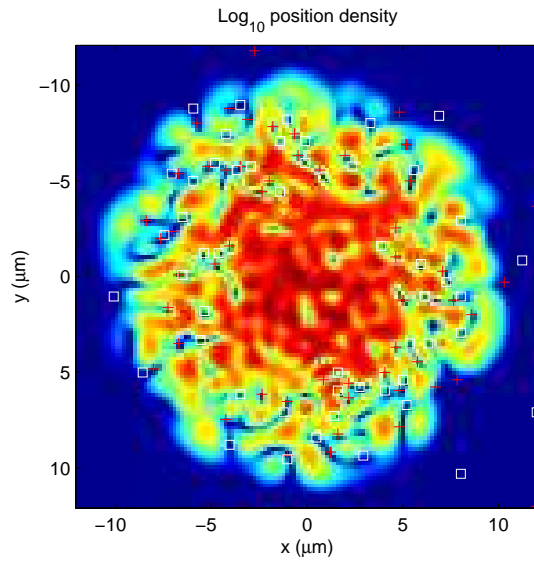


Figure 4.15: Regime D:  $T = 35$  nK, condensate fraction = 0.19

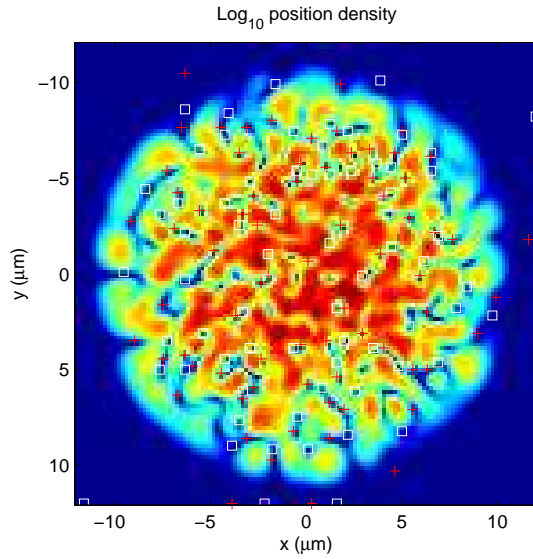


Figure 4.16: Regime D:  $T = 50$  nK, condensate fraction = 0.03

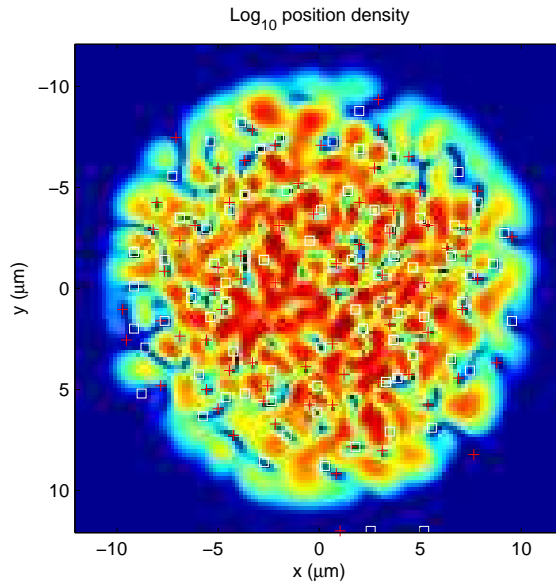


Figure 4.17: Regime D:  $T = 70$  nK, condensate fraction = 0.008

### 4.3 Vortex Pair Dynamics in BKT Regime

Here we briefly present findings displaying the behaviour of vortex pairs in the BKT regime ( $T < T^{(2)}$ ). Figures 4.18 to 4.22 are 5 consecutive frames

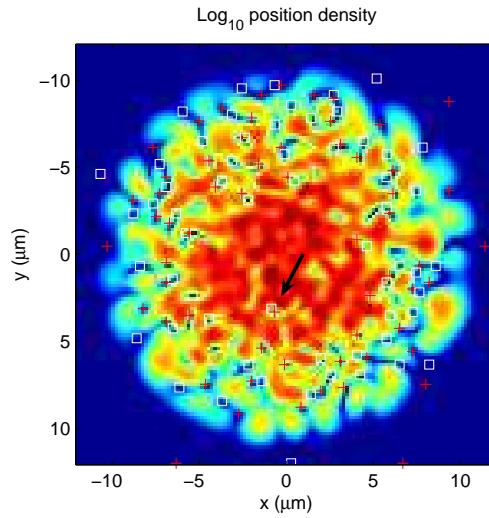


Figure 4.18: Regime D: Frame 1,  $T = 35$  nK. The black arrow indicates the vortex pair discussed in the text

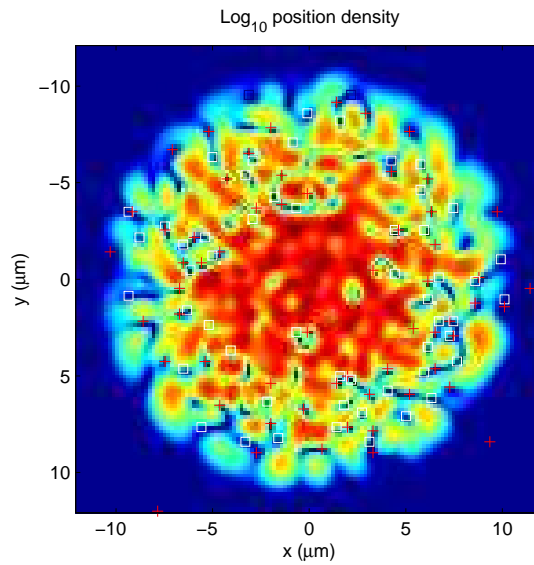


Figure 4.19: Regime D: Frame 2,  $T = 35$  nK.

showing an example of a vortex pair traversing through the the condensate centre, the lifespan of this particular pair was 8.5 ms. This phenomenon, of clearly seeing vortex pairing, is common in our simulations and provides evidence that pairs for  $T < T^{(2)}$  are long lived and are fundamental entities of this phase.

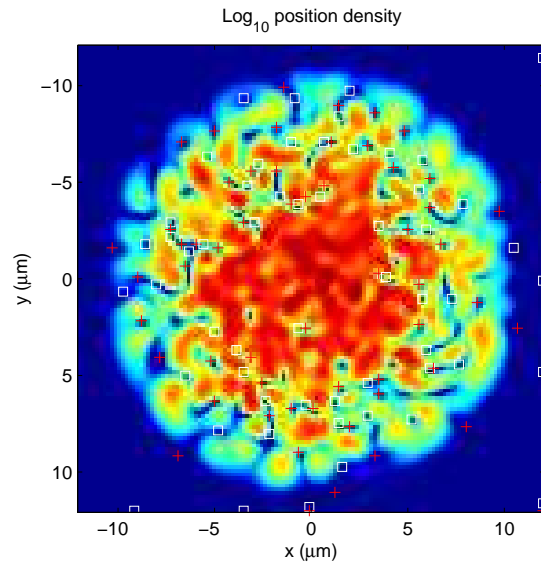


Figure 4.20: Regime D: Frame 3,  $T = 35$  nK.

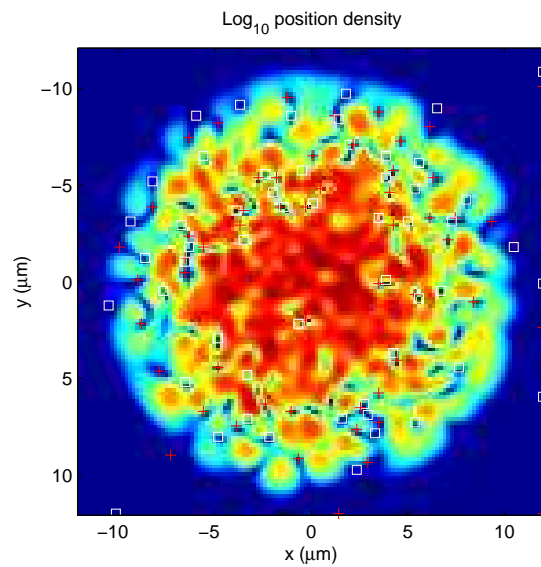


Figure 4.21: Regime D: Frame 4,  $T = 35$  nK.

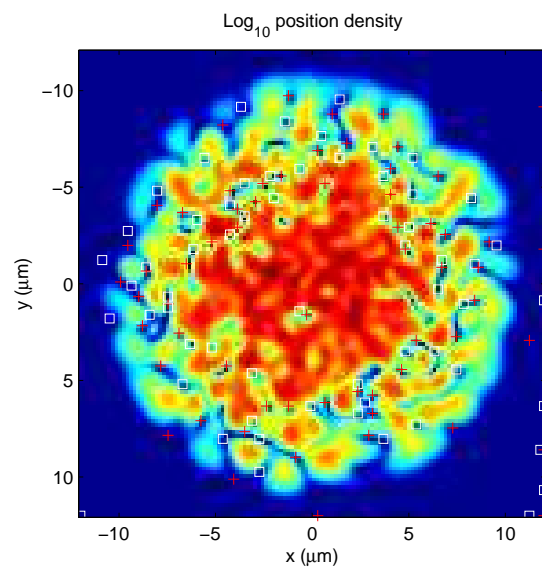


Figure 4.22: Regime D: Frame 5,  $T = 35$  nK.

# Chapter 5

## Conclusions

This dissertation begun with the introduction of 2D systems in general. We looked at known results for the ideal cases and the interacting homogenous case, then posed the question of how the interacting trapped 2D system behaves. Very little is known about these particular systems. This regime can be tested both experimentally and theoretically in the context of the ultra-cold Bose gas. Our principle aim was to investigate numerically, the behaviour of the proposed BKT transition.

We have demonstrated the pairing of vortices is a prominent feature of the BKT phase. We have also found a consistent difference between the temperature predicted for the BKT transition  $T^{(2)}$  and the temperature at the onset of bimodality  $T^{(1)}$ , which is in disagreement with the Dalibard group[12].

Our results have been central to discussions with the experimental group of Nobel Prize winner W. D. Phillips. Their group has (unpublished) experimental results with a 2D system (However, they use sodium atoms at  $\bar{f} \simeq 0.03$ ). Their results also indicate a difference between  $T^{(1)}$  and  $T^{(2)}$ .

# Chapter 6

## Appendix

Here we briefly outline work and present results of investigations concerning the choosing of the cutoff energy  $E_{cut}$ . Recall, from §3.5.3 that it is important to choose an appropriate  $E_{cut}$  such that we avoid ultraviolet divergence while still including vortices in our model, in the dense region.

The trap parameters have an isotropic loose direction trapping frequency of 9.4 Hz and a tight direction frequency of 940 Hz.

### 6.1 Cutoff Predictions

Here we use statistical mechanical arguments to predict how to adjust  $C_{NL}$  and  $E$  to maintain the same regime, whilst adjusting  $E_{cut}$ . The general idea is to approximately count the number of states between the original and new values of  $E_{cut}$ , then using the given values of  $E$  and  $n_{min}$  at the cutoff (from the original simulation), the required change in energy and number of particles is calculated to fill the newly included/excluded states. This is an approximation because we do not know the density of states or the average occupation for states distant from  $E_{cut}$ .

The results of this work are displayed in figure 6.1. Temperature is used as a measure of how much the system varies as different parameters are adjusted. The different curves represent the scenario resulting from different combinations of corrections  $C_{NL}$  and  $E$ . It was found that only the correction to energy was useful, and this method was used extensively in the following section.

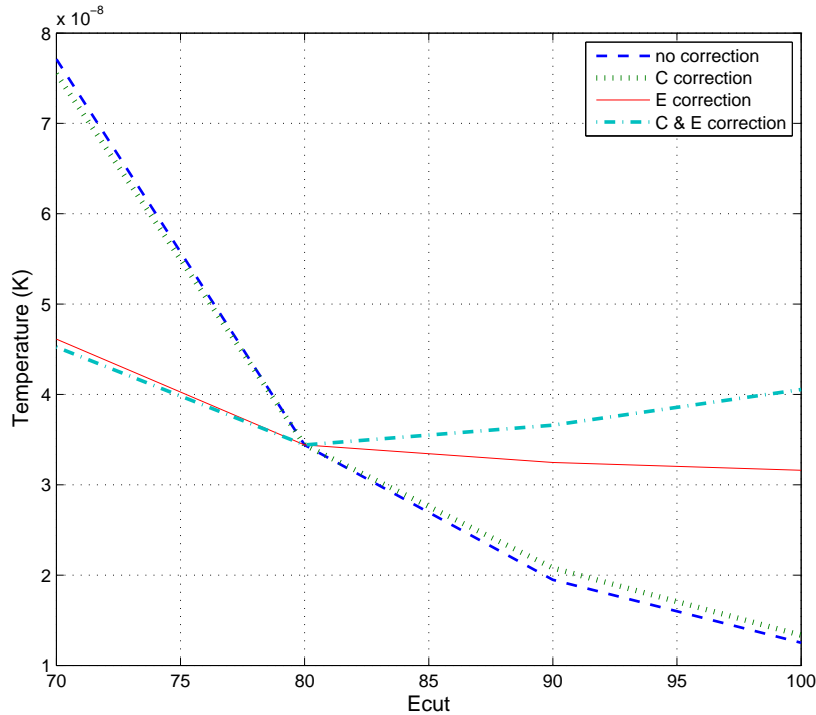


Figure 6.1:

## 6.2 Cutoff Dependence

Here, we investigate the response of a system to the variation of  $E_{cut}$  while keeping the temperature and total number of particles constant. To achieve these constants,  $C_{NL}$  and  $E$  had to be readjusted for each value of  $E_{cut}$ . This process of readjustment required many *pilot* simulations, and the code developed in §6.1 was used extensively to aid in the finding of appropriate initial conditions.

The response of the system to a change in  $E_{cut}$  was measured by the change in condensate fraction. It can be seen (figure 6.2) that the condensate fraction decreases gradually but steadily as the  $E_{cut}$  is increased. This is expected, since the rise in  $E_{cut}$  results in more of the high energy states being described classically, hence some divergence occurs which causes an increase in occupation of these high energy states, which *draws* atoms out of the condensate because the total number of atoms is fixed. We note that for the range of our prior results §4.2 ( $n_{min} = 4$  to 6) the condensate fraction does not change significantly, we also think that these values of  $n_{min}$  are

within the optimum range for CFS.

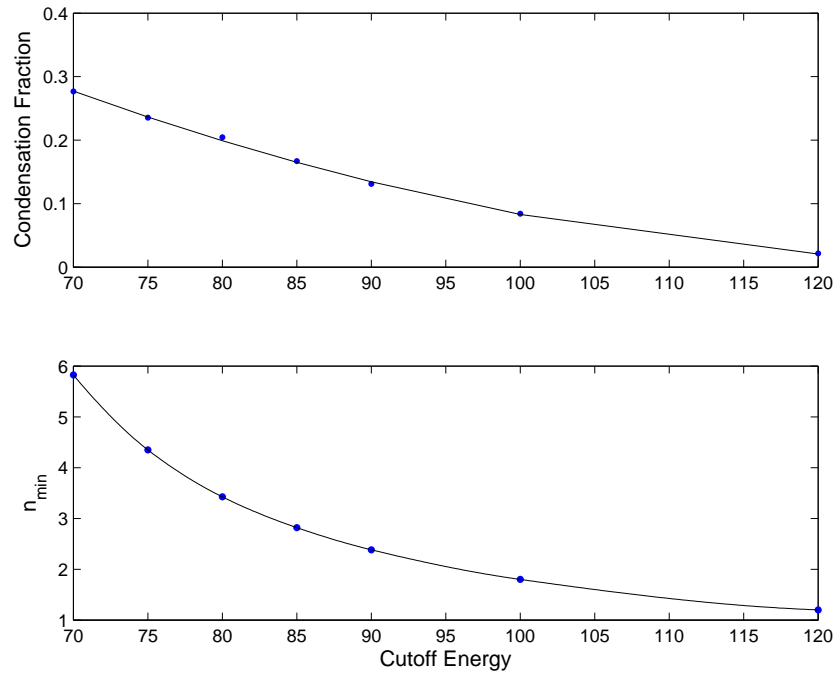


Figure 6.2:

# Bibliography

- [1] P. B. Blakie and M. J. Davis, *Projected gross pitaeviskii equation for harmonically confined bose gases at finite temperature*, Phys. Rev. A **72** (2005), 063608.
- [2] I. Bloch, J. Dalibard, and W. Zwerger, *Many-body physics with ultracold gases*, (2007), 37 – 44, arXiv:cond-mat/0704.3011v1.
- [3] M. J. Davis, R. J. Ballagh, and K. Burnett, *Dynamics of thermal bose fields in the classical limit*, J. Phys. B **34** (2001), 4487.
- [4] M. J. Davis and P. B. Blakie, *Calculation of the microcanonical temperature for the classical bose field*, J. Phys. A **38** (2005), 053615.
- [5] M. J. Davis and S. A. Morgan, *Microcanonical temperature for a classical field: Application to bose-einstein condensation*, Phys. Rev. A **68** (2003), 053615.
- [6] M. J. Davis, S. A. Morgan, and K. Burnett, *Simulations of bose fields at finite temperature*, Phys. Rev. Lett. **87** (2001), 160402.
- [7] ———, *Simulations of thermal bose fields in the classical limit*, Phys. Rev. A **66** (2002), 053618.
- [8] C. W. Gardiner and M. J. Davis, *The stochastic grosspitaeviskii equation: I*, J. Phys. B **36** (2003), 4731.
- [9] C. Gies and D. A. W. Hutchinson, *Coherence properties of the two-dimensional bose-einstein condensate*, Phys. Rev. A. **70** (2004), 043606.
- [10] Z. Hadzibabic, P. Krüger, M. Cheneau, B. Battelier, and J. Dalibard, *Berezinskii-kosterlitz-thouless crossover in a trapped atomic gas*, nature **441** (2006), 04851.

- [11] J. M. Kosterlitz and D. J. Thouless, *Ordering, metastability and phase transitions in two-dimensional systems*, J. Phys. C: Solid State Phys. **6** (1973), 1181.
- [12] P. Krüger, Z. Hadzibabic, and J. Dalibard, *Critical point of an interacting two-dimensional atomic bose gas*, (2007), arXiv:cond-mat/0703200v1.
- [13] O. Penrose and L. Onsager, *Bose-einstein condensation and liquid helium*, Phys. Rev. **104** (1956), 576.
- [14] N. Prokof'ev and B. Svistunov, *Two-dimensional weakly interacting bose gas in the fluctuation region*, Phys. Rev. A **66** (2002), 043608.
- [15] D. V. Schroeder, *Thermal physics*, pp. 315 – 319, Addison Wesley Longman, 2000.
- [16] T. P. Simula and P. B. Blakie, *thermal activation of vortex-antivortex pairs in quasi-two-dimensional bose-einstein condensates*, Phys. Rev. Lett. **96** (2006), 020404.
- [17] S. Stock, Z. Hadzibabic, B. Battelier, M. Cheneau, and J. Dalibard, *Observation of phase defects in quasi-2d bose-einstein condensation*, (2005), arXiv:cond-mat/0506559v2.
- [18] D. A. W. Hutchinson T. P. Simula, M. D. Lee, *Transition from the bose-einstein condensate to the berezinskii-kosterlitz-thouless phase*, Philos. Mag. Lett. **85** (2005), 395.